Geochemistry, Geophysics, Geosystems®

AGU ADVANCING EARTH AND SPACE SCIENCES

Key Points:

- A new, probabilistic method is presented to obtain an azimuthally anisotropic shear-velocity model from Rayleigh waves
- The model shows a two-layer anisotropic structure in the eastern Alpine crust

Correspondence to:

E. D. Kästle,
emanuel.kaestle@fu-berlin.de

Anisotropic Reversible-Jump McMC Shear-Velocity Tomography of the Eastern Alpine Crust

E. D. Kästle[1] [ORCID], **F. Tilmann[1,2]** [ORCID], **and AlpArray and Swath-D Working Groups**

[1]Institute for Geological Sciences, Freie Universität Berlin, Berlin, Germany, [2]Geoforschungszentrum GFZ Potsdam, Potsdam, Germany

Abstract The eastern Alpine crust has been shaped by the continental collision of the European and Adriatic plates beginning at 35 Ma and was affected by a major reorganization after 20 Ma. To better understand how the eastern Alpine surface structures link with deep seated processes, we analyze the depth-dependent seismic anisotropy based on Rayleigh wave propagation. Ambient noise recordings are evaluated to extract Rayleigh wave phase dispersion measurements. These are inverted in a two step approach for the azimuthally anisotropic shear velocity structure. Both steps are performed with a reversible jump Markov chain Monte Carlo (rj-McMC) approach that estimates data errors and propagates the modeled uncertainties from the phase velocity maps into the depth inversion. A two layer structure of azimuthal anisotropy is imaged in the Alpine crust, with an orogen-parallel upper crust and approximately orogen-perpendicular layer in the lower crust and the uppermost mantle. In the upper layer, the anisotropy tends to follow major fault lines and may thus be an apparent, structurally driven anisotropy. The main foliation and fold axis orientations might contribute to the anisotropy. In the lower crust, the N-S orientation of the fast axis is mostly confined to regions north of the Periadriatic Fault and may be related to European subduction. Outside the orogen, no clearly layered structure is identified. The anisotropy pattern in the northern Alpine foreland is found to be similar compared to SKS studies which is an indication of very homogeneous fast axis directions throughout the crust and the upper mantle.

Plain Language Summary The formation of the European Alps is due to the continental collision of the Adriatic and the European plates which started approximately 35 million years ago and is still ongoing. To better understand how the plates behaved during this collision process, how the crust was deformed and how distinct features like the Tauern Window were formed, we image the upper 70 km under the Eastern Alps using seismic background noise. We focus on the anisotropic shear-velocity structure of the underground, because it provides valuable additional information that can be related to the fault geometry or the main movement direction of the material. We present a probabilistic approach that attributes errors to the measured data and propagates this error through the two steps of the 3D imaging procedure, to be able to assess the uncertainty of the final model. The results show that there are two anisotropic layers in the crust, an upper crustal layer that is dominated by faster wave propagation parallel to the orientation of the mountain chain, and a lower crustal/uppermost mantle layer that has a dominantly perpendicular fast propagation direction.

1. Introduction

Seismic anisotropy describes the dependence of wavespeeds on propagation direction and wave polarization. This can be caused by anisotropic minerals but also structural features such as microcracks, shape-preferred orientation of grains or fine-scale heterogeneities (e.g., Almqvist & Mainprice, 2017; Fichtner et al., 2013; Nicolas & Christensen, 1987; Turner, 1942, and references therein). On the one hand, this relation of anisotropy on stress, strain and structural properties of the material provides valuable information on the dynamic evolution of the imaged area. On the other hand, it is very challenging to separate the different factors. Many studies concentrating on mantle anisotropy assume a relatively homogeneous composition and the dominance of olivine provides a good reason to presume that the anisotropy is largely controlled by the mantle flow (strain) (e.g., in the Alps, Barruol et al., 2011; Petrescu et al., 2020; Salimbeni et al., 2018). Lithospheric and especially crustal anisotropy is less straightforward to interpret, due to the more complex structures, rheologies and forces that act on the crust at different depth levels. Nevertheless, several studies image crustal anisotropy and relate the observations to the stress field (Guo et al., 2017; Schippkus et al., 2020), show independent dynamics of crustal layers or blocks (Agius & Lebedev, 2017; Endrun et al., 2011; Fu et al., 2016; Huang et al., 2015; Kästle et al., 2022; Soergel
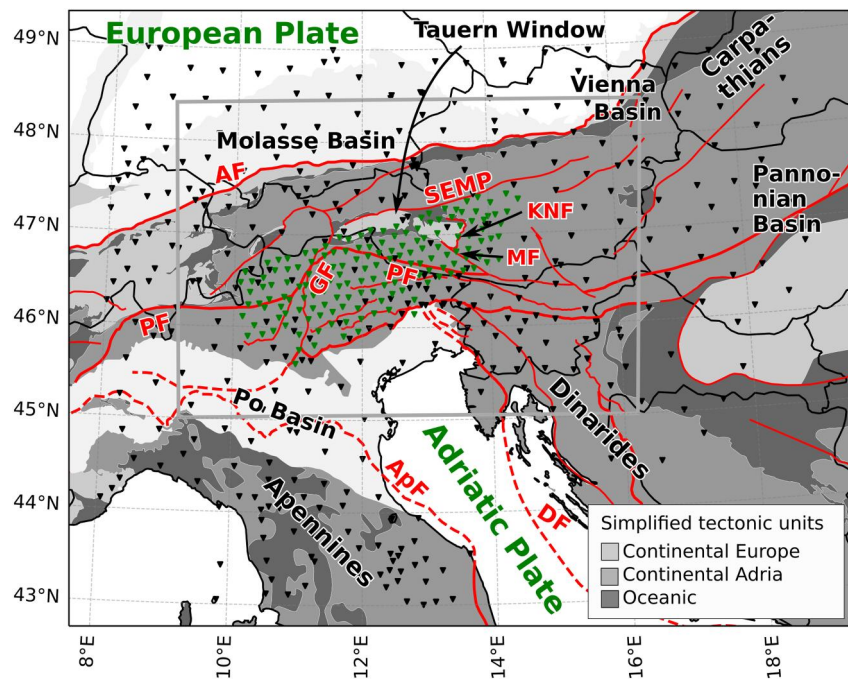
Figure 1. Tectonic overview map showing locations of permanent and temporary AlpArray stations (black triangles) and Swath-D stations (green triangles). The gray box indicates the limits of the central study region used in later images. AF Adriatic Front, ApF Apenninic Front, DF Dinaric Front, PF Periadriatic Fault, GF Giudicarie Fault, SEMP Salzach-Ennstal-Mariazell-Puchberg fault, KNF Katschberg Normal Fault, MF Mölltal Fault. Tectonic units and major lineaments simplified from Schmid et al. (2004, 2008), and Handy et al. (2010).

et al., 2022; Xie et al., 2017) or link it to subduction processes such as slab rollback (e.g., Alder et al., 2021; Fry et al., 2010; Gallego et al., 2011).

The present study targets the azimuthal anisotropy within the eastern Alpine crust (Figure 1). The Alpine mountain range results from the continental collision of the European and Adriatic plate, starting at approx. 35 Ma (Carminati et al., 2012; Handy et al., 2010, and references therein). The eastern Alpine structures underwent a major reorganization around 20 Ma: rollback subduction in the Carpathians and the opening of the Pannonian basin were accompanied by an ongoing counter-clockwise rotation of Adria (Handy et al., 2015; Le Breton et al., 2017, and references therein). The movement of the Adriatic indenter was accommodated by left-lateral strike-slip movement along the Giudicarie fault (e.g., Scharf et al., 2013). This is thought to be related to the beginning exhumation of the Tauern window and the eastward extrusion of the central Alpine crust, between the SEMP fault in the north and the Periadriatic fault in the south (Scharf et al., 2013). In this study, we examine how the seismic anisotropy observable today relates to the tectonic history, such as the different styles of collision east and west of the Giudicarie fault or the eastward crustal material flow in the central eastern Alps. There are only few examples from previous studies of the azimuthal anisotropy in the Alps (Fry et al., 2010; Kästle et al., 2022; Link & Rümpker, 2019; Schippkus et al., 2020) and only one resolving the actual depth structure of the anisotropy, albeit at low lateral resolution (Soergel et al., 2022). With the data from the dense seismic AlpArray (Hetényi et al., 2018) and Swath-D (Heit et al., 2021) networks, we are able to generate a large data set of inter-station Rayleigh-wave phase-velocity measurements from ambient noise. We follow a Bayesian inversion approach both for the phase-velocity mapping as well as for the depth inversion, so that we are able to estimate the model uncertainties and propagate them from the phase-velocity maps into the depth inversion (e.g., Bodin & Sambridge, 2009; Bodin et al., 2016).

2. Sources of Anisotropy

There are several potential mechanisms to explain seismic velocity anisotropy. At shallow depths, down to about 200 MPa (~5 km), the bulk anisotropy is assumed to be dominated by microcracks (Kern, 1990; Kern & Schmidt, 1990). In this depth range, brittle deformation is predominant and the cracks are expected to align

perpendicular to the minimum stress axis, resulting in a fast axis orientation approximately parallel to the maximum stress direction (Crampin, 1994). At greater depth, the lattice-preferred orientation (LPO, sometimes also crystallographic preferred orientation, CPO) of minerals plays an important role for the seismic anisotropy. In the mantle, the main source of anisotropy is assumed to be due to the orientation of olivine parallel to the main strain direction (e.g., Nicolas & Christensen, 1987), a mechanism often invoked to relate anisotropy to mantle flow (e.g., Barruol et al., 2011; Salimbeni et al., 2018). In the crust, the mineral assemblage is more heterogeneous, nevertheless, many minerals such as amphibole or mica will also orient their fast axis parallel to the strain direction (Barruol & Mainprice, 1993). Other effects such as the fast-axis orientation of pyroxene perpendicular to the main strain direction will counteract this anisotropy (Lamarque et al., 2016; Silver, 1996). Keppler et al. (2021) further find that microcracks which they term type I (mostly oriented along muscovite platelets) have a major influence on the anisotropic amplitude and are fully closed only at pressures of 740 Mpa (∼25 km). They thus imply a strong dependence of this type of anisotropy on depth, with effective anisotropies for an average Alpine crustal rock model ranging from 12% close to the surface to about 4% in the lower crust where microcracks are completely closed. Similarly, Zertani et al. (2020) report an expected effective anisotropy of ∼4% for an eclogite facies effective medium. The experimentally determined fast axis are approximately oriented in the foliation plane and in lineation direction, that is, approximately in strain direction, even though there may be a discrepancy between quartz lineation and the orientation of mica crystals depending on the rock type (Keppler et al., 2021). Next to microcracks and LPO, there are more microstructural effects that potentially influence the anisotropy such as shape preferred orientation (SPO) of grains, grain boundaries distribution of mineral grains or deformation lamellae (Almqvist & Mainprice, 2017). On the macro-scale, additional complexities arise since folds and faults may form complex patterns of foliation and layering. Okaya et al. (2019) show that typical geological structures can significantly influence the bulk anisotropy measured with long wavelength signals and produce more complex and differently oriented anisotropies compared to the anisotropy of the rock sample at microscale. Thus, seismologists sometimes distinguish between intrinsic and apparent anisotropy (e.g., Alder et al., 2017; Fichtner et al., 2013). Intrinsic describes the strain-controlled LPO of minerals while the apparent anisotropy is controlled by the aforementioned micro- and macrostructures such as cracks, faults or layers that form structural and chemical heterogeneities. These heterogeneities may be isotropic per se, but if they are below the resolution limit of the applied tomographic method they produce an apparent anisotropy. Extending the ideas of Backus (1962) and Fichtner et al. (2013) show that for most effective anisotropic media, a purely isotropic counterpart with fine layering can be found that would yield the same apparent anisotropy. Both intrinsic and apparent anisotropy carry relevant information on the structure and the dynamic evolution through information on strain (LPO) or stress (shallow microcracks). They cannot be distinguished on the basis of seismic data alone, except, theoretically, that some combinations of anisotropy parameters require the presence of intrinsic anisotropy.

The present study is limited to the analysis of Rayleigh waves for which we assume the medium to be horizontal transversely isotropic (anisotropy is assumed to have a horizontal symmetry axis). With additional information, such as Love waves, it would be possible to obtain also information on the radial anisotropy and the more general case of a tilted symmetry axis (e.g., Xie et al., 2015). In nature, the elastic tensor may be even more complex, cases of non-elliptical elastic tensors and related ambiguities are discussed in Erdman et al. (2013), Xie et al. (2015), Brownlee et al. (2017), and Okaya et al. (2019). In this work, we will discuss possible interpretations of the effective, apparent azimuthal anisotropy in the context of known structural and geodynamic features such as fault orientations and the predominant compression direction.

3. Methods

3.1. Phase-Velocity Measurements

This study is based on ambient-noise recordings from more than 2 years. Phase velocities for Rayleigh waves are obtained from stacked Z-component cross correlations with the zero-crossing method (Aki, 1957; Ekström et al., 2009; Kästle et al., 2016). The pre-processing and phase-velocity extraction steps are slightly modified from Kästle et al. (2022) and Magrini et al. (2022) by including the idea of Green et al. (2020) in using monthly stacks. A more detailed description can be found in the supplement to this article. The total data set comprises 84,905 inter-station phase-velocity measurements, of which 33,657 involve Swath-D stations (compare Figure 1).

3.2. Azimuthally Anisotropic Transdimensional Phase-Velocity Tomography

Bodin and Sambridge (2009) present a method for surface-wave tomography in a Bayesian framework which is implemented for this study. In this approach, the model space (2D phase-velocity map) is parameterized using Voronoi cells whose number is not fixed during the inversion and controlled by the data and the data uncertainty, hence the denomination transdimensional. It applies a reversible jump Markov chain Monte Carlo (rj-McMC) algorithm to perform a random walk through the parameter space drawing samples from the posterior probability distribution $p(\mathbf{m}|\mathbf{d}^{obs})$, that is, the probability density of model parameters $\mathbf{m}$, given our observed data $\mathbf{d}^{obs}$. According to Bayes' theorem, the posterior distribution is related to the likelihood function $p(\mathbf{d}^{obs}|\mathbf{m})$ and the prior on the model parameters $p(\mathbf{m})$, as

$$p(\mathbf{m}|\mathbf{d}^{obs}) \sim p(\mathbf{d}^{obs}|\mathbf{m})\, p(\mathbf{m}). \tag{1}$$

In order to include azimuthal anisotropy in this approach it is necessary to assign an anisotropic fast axis amplitude a_2 and its orientation Ψ_2 to each Voronoi cell. The model vector is thus $\mathbf{m} = \left\{\left(\mathbf{x}^{(1)}, c_0^{(1)}, a_2^{(1)}, \psi_2^{(1)}\right), \ldots, \left(\mathbf{x}^{(M)}, c_0^{(M)}, a_2^{(M)}, \psi_2^{(M)}\right)\right\}$ where M is the number of Voronoi cells. The parameter $\mathbf{x}^{(i)}$ gives the (x, y) coordinate location of the ith Voronoi nucleus. The azimuthally anisotropic phase velocity c_{AA} for weakly anisotropic media depends on the wave propagation direction Φ and can be expressed as

$$c_{AA}(\Phi) = c_0[1 + a_2 \cos(2(\Phi - \Psi_2))] = c_0[1 + c_1 \cos(2\Phi) + c_2 \sin(2\Phi)], \tag{2}$$

where $c_1 = a_2 \cos(2\Psi_2)$ and $c_2 = a_2 \sin(2\Psi_2)$. We only account for the Ψ_2-anisotropy which should be the dominant component in Rayleigh wave propagation (Montagner & Nataf, 1986). In principle, it would be possible to add the Ψ_1 (360° periodicity) and the Ψ_4 (90° periodicity, relevant for Love waves) anisotropic components in the same way, but that would result in much longer computation times for the model search due to the additional free parameters and would create more ambiguity in the interpretation due to trade-offs.

In each iteration, the algorithm chooses from one of several possible model updates: (a) update one of the parameters (c_0, a_2, ψ_2) in one of the Voronoi cells, (b) create an additional, isotropic Voronoi cell with a randomly chosen velocity (birth), (c) delete an existing, isotropic Voronoi cell (death), (d) move the nucleus ($\mathbf{x}$) of one of the Voronoi cells, (e) add azimuthal anisotropy to an existing, isotropic cell, (f) remove the azimuthal anisotropy from an existing, anisotropic cell, (g) update the hyperparameters (see below). These steps are defined following Bodin et al. (2016): each birth operation of a Voronoi cell will create an isotropic cell to which anisotropy can be added in a later step while at the same time a death operation of a cell is only applicable to isotropic cells. Of course, updates of a_2 and ψ_2 are only performed in anisotropic cells. Adding more cells or adding anisotropy to an existing cell increases the likelihood. This is counter-acted by the prior probability which is reduced by the additional complexity. The algorithm thus prefers the simplest model that is able to explain the data with the given data uncertainty and should only add anisotropy where it is required by the data. For more details and the exact terms for the acceptance probabilities of the different steps, please see Bodin et al. (2016).

We follow the approach of Tilmann et al. (2020) who describe the likelihood as a combination of a Gaussian and a bounded uniform distribution. This can help to reduce the influence of outliers on the resulting phase-velocity maps. For a total of N measurements it reads

$$p(\mathbf{d}^{obs}|\mathbf{m}) = \prod_{i=1}^{N}\left[(1-f)\frac{1}{\sqrt{2\pi}\,\sigma}\exp\left(-\frac{r_i^2}{2\sigma^2}\right) + f\frac{1}{W}\right], \tag{3}$$

where r are the residuals between measured and modeled data for the currently proposed model. As Bodin and Sambridge (2009), it is assumed that the individual measurements are uncorrelated. The above equation contains the two noise hyperparameters that are treated as unknown in the model search (hierarchical approach, Gelman et al., 1995), σ for the data standard deviation (in km/s) and f for the fraction of outliers. The width of the uniform distribution W describing the outliers is pre-defined as suggested by Tilmann et al. (2020).

After each model update, the forward problem has to be solved to compute synthetic data and obtain the residuals. Details on the forward calculation are provided in the supplement to this article. The modeled data is calculated
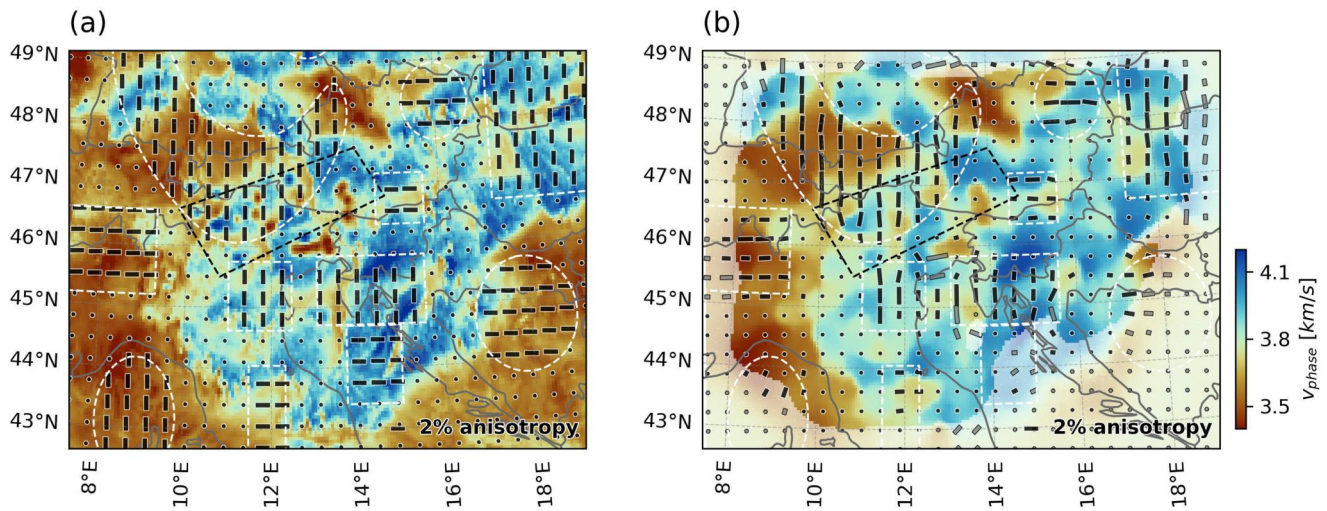
Figure 2. Synthetic example at 8 s period where (a) shows the input model that includes azimuthally anisotropic patches, surrounded by white outlines, whose fast axis are oriented either N-S or E-W as indicated by black bars. All input anisotropies have $a_2 = 0.02$, that is, 2%. (b) Recovered model where the fast-axis bars colored in gray indicate a high uncertainty (see text). Regions where the uncertainty in the isotropic velocity exceeds 0.1 km/s are shown in muted colors. Anisotropic fast axis with an uncertainty $\sigma_{aniso} > 0.03$ are plotted in gray. The colorbar and anisotropic fast axis scaling are identical for both panels. The measurement geometry is the same as in Figure 3a. The region of the very dense Swath-D network is highlighted with a black dashed line. Tests for at other periods are shown in the supplement to this article.

along ray paths that are traced in the mean, anisotropic velocity model. The anisotropic Fast Marching Method described in Chen et al. (2023) is used to obtain travel time fields for all source stations. The rays are traced along the steepest gradient in the travel time fields from the receivers back to the source stations.

3.3. Priors and Model Search Parameters

In this work, we perform 100 parallel model searches, each running for 500,000 iterations of which the first 200,000 are discarded as burn-in steps. Only every 500th model is kept for computational reasons, which corresponds to only minimal loss of information as subsequent models in each chain are strongly correlated. The ray paths are re-calculated every 80,000 iterations using the average anisotropic model from all searches. The priors are all uniform distributions with the following boundaries: $c_0 = [0.5 \cdot \min(c_{interstation}), 1.5 \cdot \max(c_{interstation})]$ where $c_{interstation}$ are the measured phase velocities between station pairs, $a_2 = [0, 0.1]$, $\Psi_2 = [-90°, 90°]$, $\sigma = [0.01, 1.0]$, $f_{outlier} = [0, 0.8]$, and the number of Voronoi cells is limited between 10 and 5,000. The model searches are initiated with 100–500 isotropic Voronoi cells with random phase-velocity parameters. The initial data standard deviation σ is set to 0.5 km/s and the initial outlier fraction $f_{outlier}$ is 0.1 (10%). The model updates for phase velocity perturbations and changes in the cell positions are optimized such that the acceptance rate is kept around 45%. For birth proposals, the velocity in the newborn cell is chosen randomly from within the prior range, which has been shown to result in good model mixing (Dosso et al., 2014).

In the following phase-velocity map plots, we define a measure for the uncertainty of the anisotropic measurements using the posterior standard deviations of c_1 and c_2 as

$$\sigma_{aniso} = \sqrt{\sigma_1^2 + \sigma_2^2}. \tag{4}$$

This measure combines the uncertainty in the amplitude and the direction of the fast axis. It is used to categorize the fast axis measurements in the phase-velocity maps, but has no influence on the results of the depth inversion.

3.4. Synthetic Example

The synthetic data for the test presented in Figure 2 is calculated along rays in the anisotropic input model. A Gaussian error with standard deviation of 0.02 km/s is added to the calculated path average phase velocities. Additionally, we added a uniformly distributed error of up to ±0.5 km/s to 5% of the measurements to simulate outliers. The model search correctly recovers the input data standard deviation of 0.02 km/s whereas the outlier
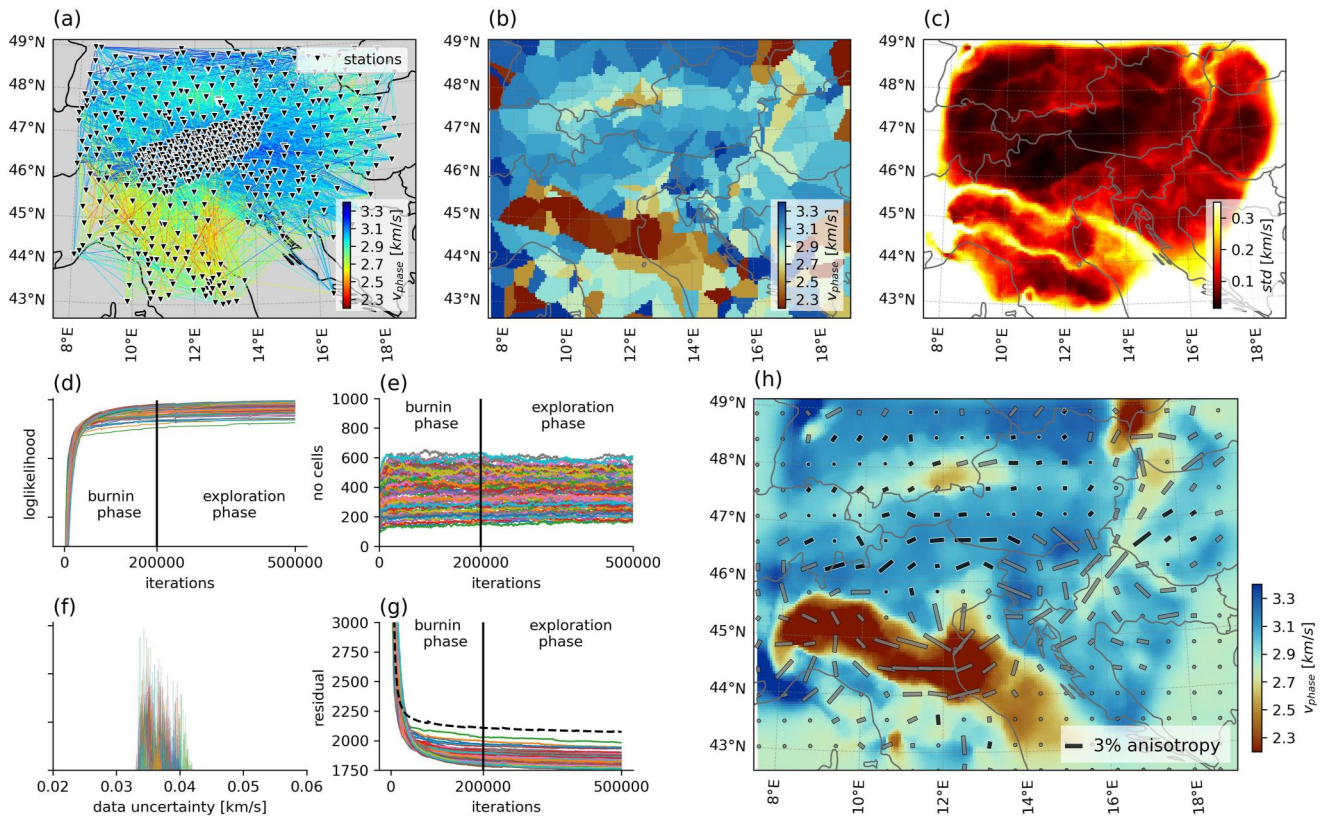
Figure 3. Phase velocity tomography with the rj-McMC method for the Rayleigh-wave data set at 8 s period. (a) Distribution of seismic stations and inter-station phase-velocity measurements. (b) Example of an isotropic Voronoi cell model at one random iteration in the exploration phase. (c) Isotropic model standard deviation. (d) Loglikelihood curves of the 100 chains. The ray geometry is updated every 80,000 iterations causing small kinks. (e) Evolution of the number of cells of the 100 chains. (f) Histogram of the data standard deviation (hierarchical search parameter). (g) Evolution of the data residuals over 500,000 iterations. The dashed line shows the average residual for an isotropic search. (h) Average of all accepted Voronoi models from a total of 100 chains. Anisotropic fast axis with an uncertainty $\sigma_{aniso} > 0.03$ are plotted in gray.

fraction is estimated to be smaller with only ∼2%. The recovered, isotropic part of the model is smoother compared to the input model. The circular anomalies of approx. 25 km diameter are at the resolution limit of the model with the given data uncertainty. The anisotropy is correctly recovered inside the patches, apart from the model boundaries where there is no data coverage. Note that large velocity contrasts correlate with a higher uncertainty in the anisotropy, which we relate to a trade-off between the isotropic and anisotropic components. This can be a problem at the model boundaries where the azimuthal coverage is bad and thus more spurious anisotropy is imaged.

3.5. Real Data Example

The data set at 8 s period comprises 57,203 inter-station phase-velocity measurements (26,534 of those involving Swath-D stations) whose data standard deviation is estimated by the algorithm to be ∼0.035–0.04 km/s and the fraction of outliers to be ∼4% (Figure 3). The largest model standard deviations in the isotropic velocities correlate with the model boundaries and strong velocity contrasts such as around the Po basin. The data uncertainty, likelihood and residual of all chains converge to very similar values after only 100,000 iterations. The remaining spread correlates approximately with the number of cells, that is, more cells give a lower residual, and lower estimated data uncertainty. The relative stability in the number of cells indicate that there are many local minima to which the chains converge. It is unlikely that individual chains jump between models of completely different numbers of cells. Only models with very large or very small numbers of cells are excluded by the algorithm. We confirmed this behavior by comparison with the (isotropic) rj-TOMO code (iearth.edu.au/codes/rj-TOMO/, v.0.9.16, e.g. used in Bodin and Sambridge (2009)). It seems to be a general property of the Voronoi-
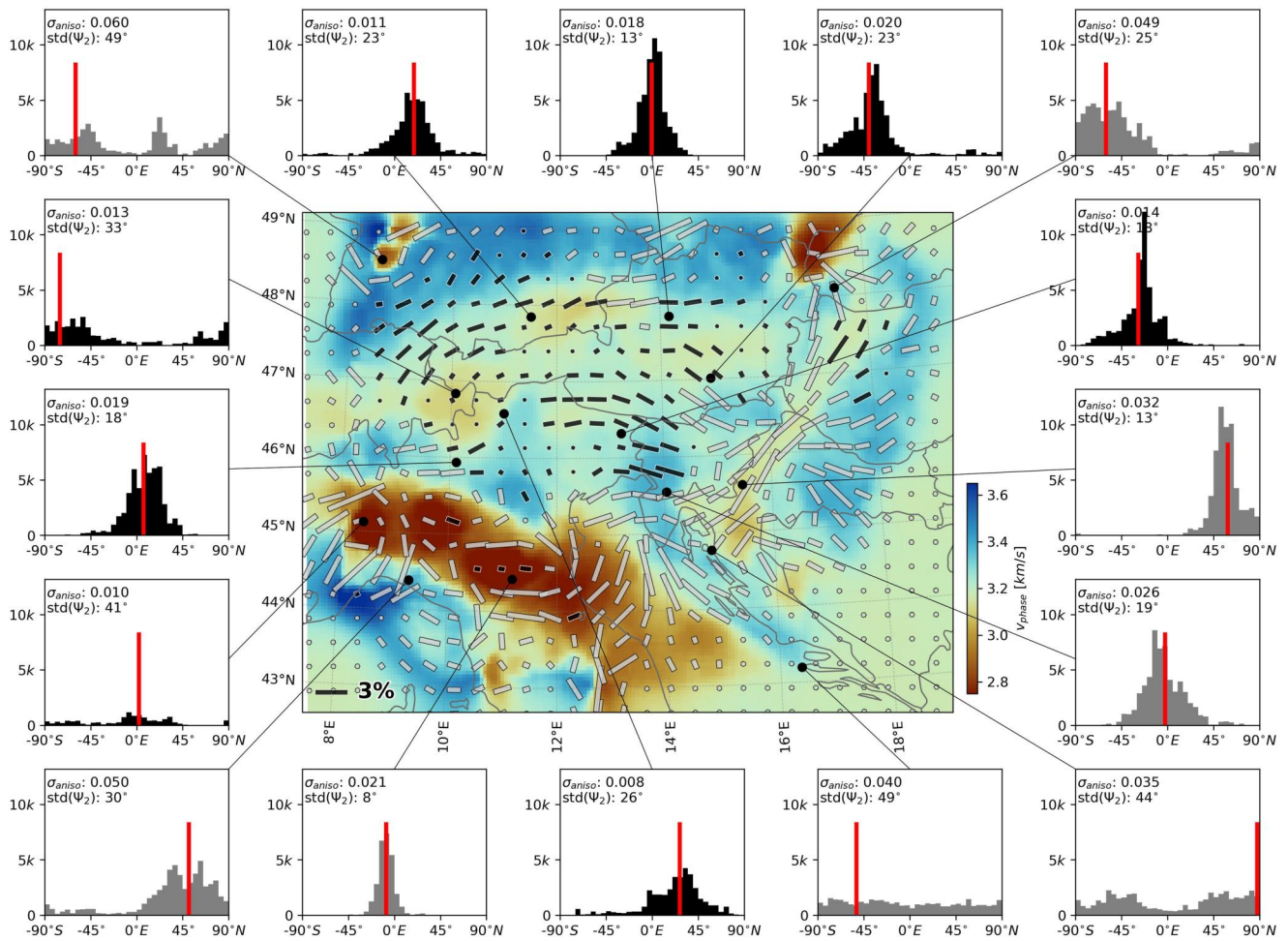
Figure 4. Anisotropic phase-velocity map at 15 s period. The map in the center shows the imaged distribution of Rayleigh phase velocities, the black bars indicate amplitude (a_2) and direction (Ψ_2) of the mean anisotropic fast axis. The fast axis bars and corresponding histograms are grayed out if the uncertainty $\sigma_{aniso} > 0.03$ (Equation 4). The panels surrounding the map give histograms of the fast axis directions from all accepted models where the amplitude $a_2 > 0.5\%$. The red lines give the final, mean direction which is plotted in the map.

based rj-McMC method with large data sets, a large numbers of unknowns and data uncertainty being included as unknown in the rj-McMC.

Using the fast-axis directions from the accepted models, we test for the robustness of the final, mean directions (Figure 4). The mean fast axis directions and amplitudes result from the average vector of all accepted fast axis. This means that isotropic cells ($a_2 = 0$) lower the average anisotropic amplitude but do not influence the average direction. The analyzed points in the center of the map show clear, single-peaked distributions of the fast-axis directions. This shows that all chains converge to the same solution. Exceptions are found at the model boundaries, where the data coverage is low or even zero. Where two regimes with different anisotropic orientations meet, bi-modal distributions may appear. This is related to small variations in the Voronoi geometry when iterating through alternative models, analog to the isotropic case at the border of the Po basin in Figure 3c. In regions without data coverage, the prior (flat distribution) is recovered. For the depth inversion step, the mean c_1 and c_2 parameters (Equation 2) and their standard deviations σ_1 and σ_2 are passed on. If the distribution is non-Gaussian, this may introduce an error. However, since the standard deviation is typically large in these cases, it will only have a small effect on the final result. Future applications may profit from passing on the complete posterior distribution as prior to the depth inversion.

3.6. Depth Structure Inversion

We invert for the depth-dependent 1D shear-velocity profiles using a version of the BayHunter software (Dreiling & Tilmann, 2019) modified to include azimuthal anisotropy. It implements a rj-MCMC algorithm according to the same principles as laid out in Section 3.2. A short summary of the method is given in the following, specific to our inverse problem, for a more complete overview of the method see Bodin et al. (2012, 2016) and the documentation of BayHunter (Dreiling & Tilmann, 2019).

For each model grid cell we construct an anisotropic Rayleigh dispersion curve from the phase velocity maps. Again, we assume a weakly anisotropic medium so that the azimuthally anisotropic shear velocity can be written as

$$\mathbf{v}_S(z, \Phi) = \mathbf{v}_{S,iso}(z)[1 + \mathbf{a}_2(z)\cos(2(\Phi - \mathbf{\Psi}_2(z)))]. \tag{5}$$

The depth model is parameterized in terms of layers with constant model parameters in each layer. The number and thickness of the layers is variable and given by a nearest neighbor interpolation from the depth of the nucleii $\mathbf{z} = (z_1, \dots z_M)$. The v_P/v_S ratio is not well constrained without additional information such as from Love phase velocities. We therefore fix the v_P/v_S ratio to 1.73 in the crust and 1.8 in the mantle. The density is given by an empirical relation $\rho = 0.32 v_P + 0.77$ (Berteussen, 1977). The model vector contains the remaining, free parameters $\mathbf{m} = (\mathbf{z}, \mathbf{v}_S, \mathbf{a}_2, \mathbf{\Psi}_2)$.

The input data is given by the mean of the isotropic and the two anisotropic phase-velocity components $\mathbf{c}_0(T)$, $\mathbf{c}_1(T)$, and $\mathbf{c}_2(T)$ and their respective standard deviations $\boldsymbol{\sigma}_0(T)$, $\boldsymbol{\sigma}_1(T)$, and $\boldsymbol{\sigma}_2(T)$, which are only defined at a set of distinct periods T, where phase velocities were measured and the 2D tomography carried out. The same basic steps as for the phase-velocity mapping are applied: Updating parameters in a single layer, adding/removing an isotropic layer, adding/removing anisotropy to an existing layer. Since we do not include outliers and fix the data standard deviations, no hyperparameter updates are performed. The likelihood function for the depth inversion reads

$$p(\mathbf{d}^{obs}|\mathbf{m}) = \frac{1}{\prod_i \sqrt{2\pi}\sigma_{0,i}} \frac{1}{\prod_i \sqrt{2\pi}\sigma_{1,i}} \frac{1}{\prod_i \sqrt{2\pi}\sigma_{2,i}} \exp\left(-\sum_i \frac{(g_{0,i}(\mathbf{m}) - c_{0,i})^2}{2\sigma_{0,i}^2}\right.$$
$$\left. -\sum_i \frac{(g_{1,i}(\mathbf{m}) - c_{1,i})^2}{2\sigma_{1,i}^2} - \sum_i \frac{(g_{2,i}(\mathbf{m}) - c_{2,i})^2}{2\sigma_{2,i}^2}\right) \quad . \tag{6}$$

The anisotropic forward modeling performed by function $g(\mathbf{m})$ is based on the works of Montagner and Nataf (1986), Bodin et al. (2016), and Liu et al. (2019), and is described in the supplement to this article.

3.7. Depth Inversion Priors and Search Parameters

At each grid point, we perform 20 model searches (chains) in parallel that run for 150,000 iterations of which the first 50,000 iterations are discarded as burn-in samples. The model search starts with a purely isotropic model and anisotropy is only added after 25,000 iterations. This helps to reduce the computation time and has otherwise no significant effect on the result according to our tests. The priors for the search parameters are given by uniform distributions with the limits $v_S = [1.5, 5]$, $a_2 = [0, 0.1]$, $\Psi_2 = [0, 180°]$, and the number of layers may vary between 3 and 10. The uncertainties $\sigma_{(0,1,2)}$ from Equation 6 are fixed to the values obtained from the phase velocity maps. The model search is limited to a maximum depth of 120 km and the deepest layer always represents the half space. We limit the range of possible models by only accepting those with a Moho discontinuity, here defined as a jump from $v_S \leq 4.1$ to $v_S \geq 4.2$. Above the Moho, the velocity differences between adjacent layers are limited to -0.5 km/s $< \Delta v_S < 0.8$ km/s (with increasing depth), and below to $|\Delta v_S| < 0.3$ km/s. The effect of these choices is discussed below and alternative models are presented in the supplement.

3.8. Depth Inversion Example

The result of the model search for a profile located at 46.5°N/13.5°E is presented in Figure 5. The likelihood and the joint misfit are approximately stationary after the burn-in phase. The kink in the likelihood and residual curves at −25,000 iterations is caused by adding the anisotropic parameters. Every 20th model from each chain is kept
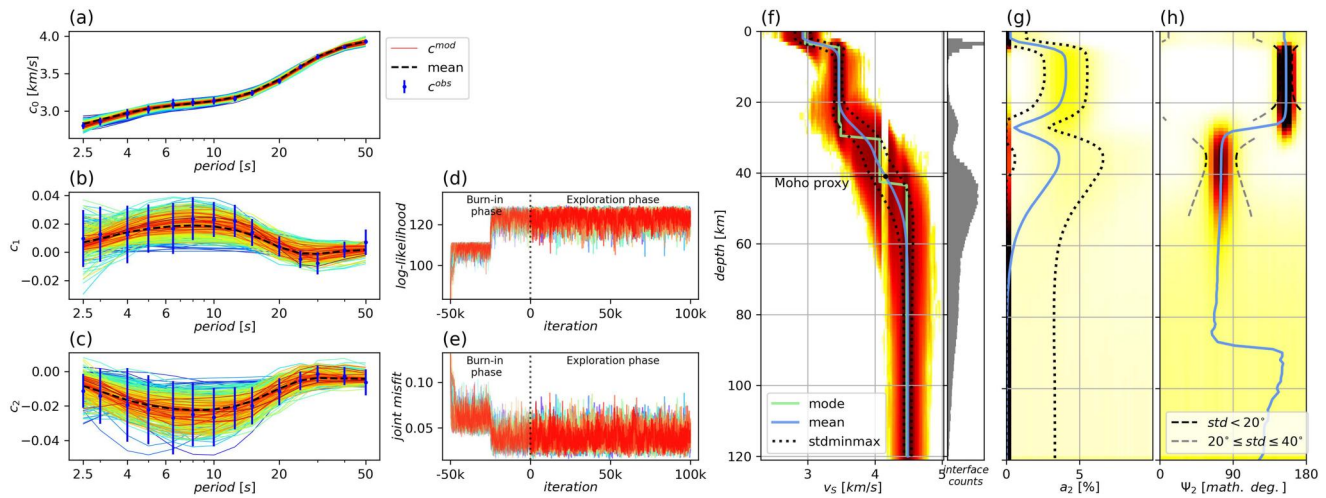
Figure 5. Example depth inversion at 46.5°N/13.5°E. (a) Observed Rayleigh phase velocity and error bars defined by the standard deviation σ_0 from the phase-velocity maps. Modeled dispersion curves are colored according to their misfit. The dashed line gives the mean of all models. (b and c) Same for the c_1 and c_2 components. (d) Log-Likelihood evolution over 150,000 iterations (Equation 6). The colors correspond to the 20 chains. The anisotropic parameters are only added after −25,000 iterations, causing the jump in the likelihoods. (e) Joint rms misfit evolution, same color coding as previous panel. (f) Histogram of v_S values obtained during the exploration phase shown as heatmap (logarithmic color scale). The panel on the right gives the number of velocity interfaces in the depth range. The scarcity of models with velocities 4.1–4.2 km/s arises from the prior condition of a Moho discontinuity straddling these velocities, see text. (g and h) Shows the same for the a_2 and the Ψ_2 components. Note that for depths larger than ∼50 km the probability mass is strongly concentrated at the left of the plot, indicating 0% anisotropy. The maximum standard deviation in the anisotropy direction is ∼50° for a uniform distribution between 0° and 180°.

which leads to a final number of 100,000 models. In the example, two anisotropic layers with amplitudes around ∼3%–4% are needed to fit the data. The anisotropic amplitudes are not tightly constrained, but the fast axis directions vary only in a narrow band in the two anisotropic layers. At periods above 20 s, the c_1 and c_2 parameters are close to zero, therefore, no deeper anisotropic layer is needed in the depth model, and the probability distribution for the anisotropy amplitude is peaked strongly at 0% anisotropy.

4. Results

4.1. Phase-Velocity Maps

Phase velocity maps are calculated at periods T = [2.5, 3, 4, 6.5, 8, 10, 12.5, 15, 20, 25, 30, 40, 50] of which a selection is shown in Figure 6. The isotropic velocity distributions show clear structural patterns at short periods that can be related to the sedimentary basins north and south of the Alps. At longer periods, they indicate regions of thickened crust underneath the orogen. The anisotropic fast axis are mostly E-W oriented within the Alps at periods up to 12.5 s. At longer periods, the fast axis in the central Alps rotate to a N-S direction, while the structure in the eastern Alps is more complex and remains rather E-W oriented. At 6.5 s, the orientation of the fast axis seems to follow closely the Periadriatic and the Giudicarie faults (Figure 1). The estimated data uncertainties are approximately 0.04 km/s at the shortest period of 2.5 s, decrease with increasing period to a value 0.03 km/s where they remain at periods 10–20 s and increase again toward long periods to a maximum of 0.06 km/s at 50 s. This variation is typical for ambient noise measurements, where short period data is affected by stronger velocity heterogeneities and stronger attenuation. The highest quality measurements are found around the microseismic peaks (7–20 s), whereas the quality decreases again toward longer periods where the noise amplitudes are lower but also the ray approximation introduces errors in the forward modeling. Therefore, we observe the highest uncertainty in the phase velocity maps at short periods both in the isotropic and the anisotropic components and the lowest uncertainty at intermediate periods (15–20 s). At the long period end, the uncertainties do not increase significantly, because the total velocity variability is rather low.

4.2. Shear-Velocity Model

Since the inversion of the depth-dependent shear-velocity profiles is computationally demanding, the model area is reduced to the well resolved area between 9–16.5°E and 45–48.5°N and resampled using a linear interpolation
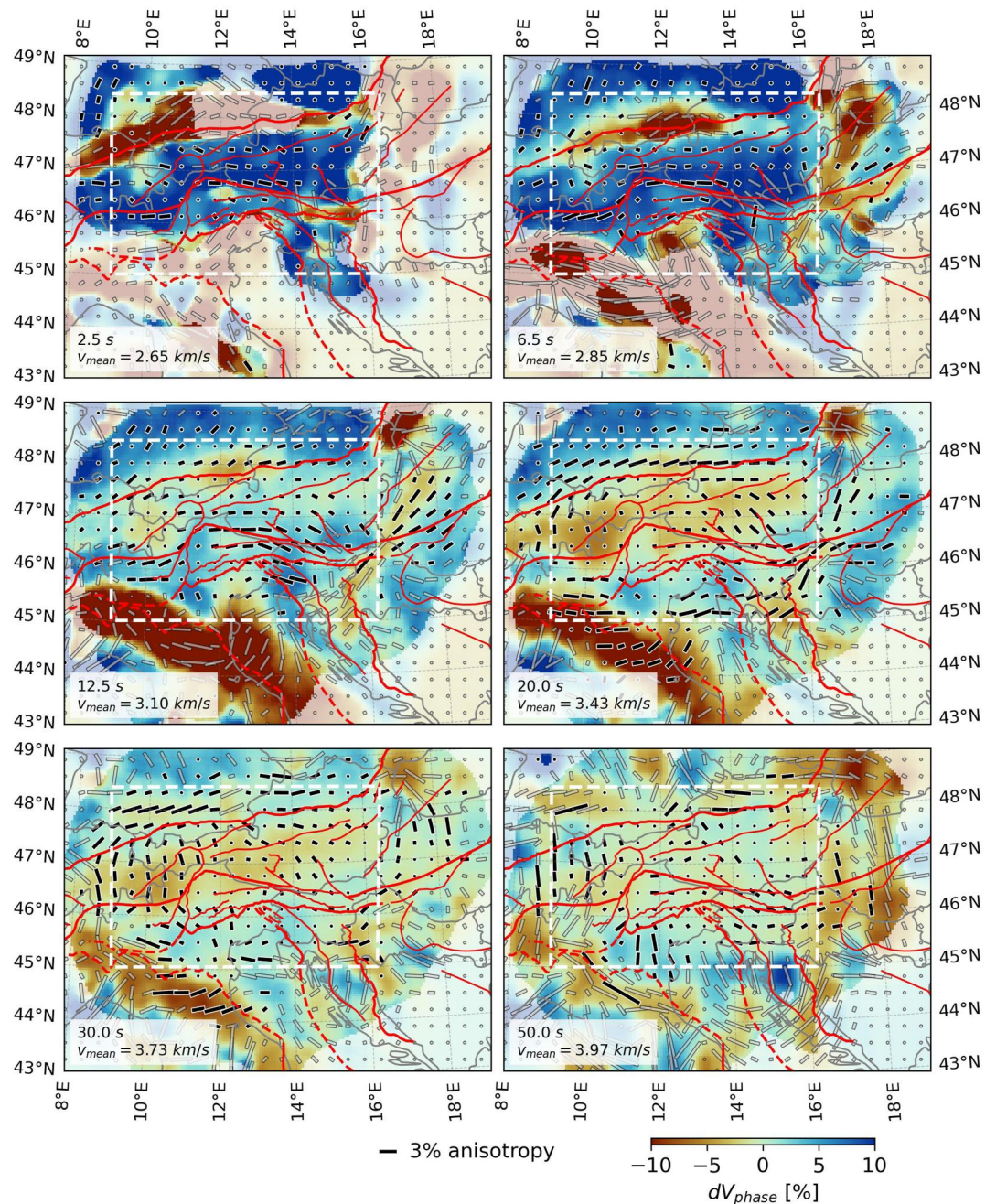
Figure 6. Rayleigh fundamental mode phase-velocity maps at selected periods. Velocities are given as deviations from the mean velocity shown in the bottom left corner of each panel. Black bars indicate the direction and amplitude of the azimuthal anisotropy fast axis. Grayed out bars indicate that the anisotropy uncertainty exceeds 0.03 (Equation 4, Figure 4). Regions where the isotropic velocity uncertainty is greater 0.2 km/s are shown with the colors blended to white. Maps showing the isotropic velocity uncertainties for these maps are given in Figure S6 of the Supporting Information S1. The dashed box outline indicates the region where the depth inversion is performed. Tectonic lineaments in red are simplified from Schmid et al. (2004, 2008), and Handy et al. (2010).

(no additional smoothing or averaging) from an originally 5×5 km gridspacing to a $0.1 \times 0.125°$ (lon $\times$ lat, i.e., $\sim 10 \times 10$ km) spacing. This results in 2196 model points at which $\mathbf{c}_{iso}(T)$, $\mathbf{c}_1(T)$, and $\mathbf{c}_2(T)$ and their standard deviations are extracted and inverted. The anisotropy in the shear-velocity model in Figure 7 is not shown at locations where the standard deviation in the fast-axis direction is greater $40°$ (Figure 5). Note that a uniform distribution between -90 and $90°$ would result in a standard deviation of $\sim 50°$, that is, no information gain on the
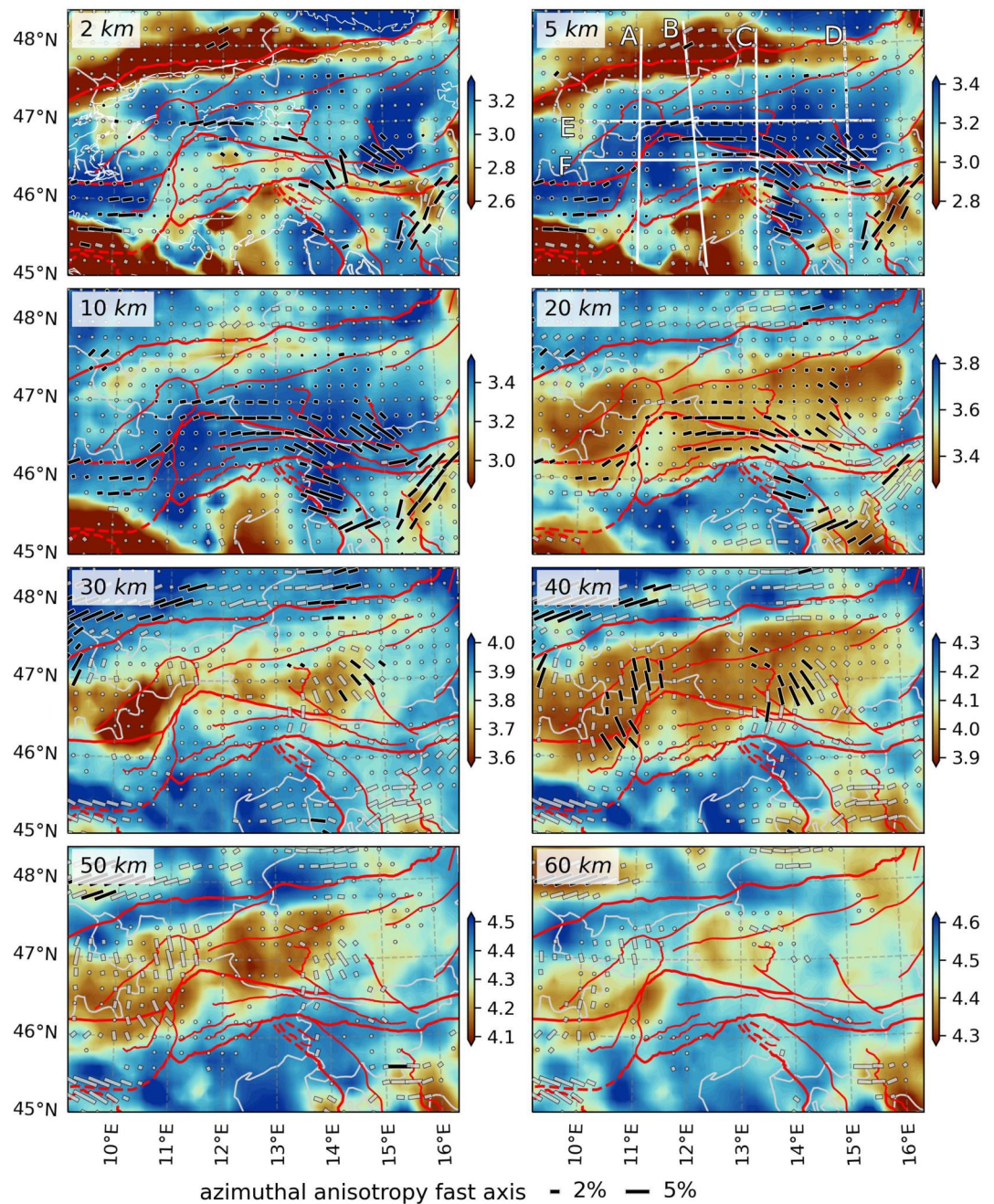
Figure 7. Azimuthally anisotropic shear-velocity maps at different depth levels. The color scales give the isotropic shear velocity in km/s. The bars indicate the anisotropic fast axis amplitudes and directions. No fast axes are shown if the directional standard deviation is greater than 40°, a gray bar means that the standard deviation is between 20 and 40° and a black bar is plotted if the standard deviation is below 20°. The three standard deviation intervals correspond to those shown in Figure 5h. The red lineaments are the same as in Figure 6. Additional white lines in the map at 2 km depth give the outlines of the major tectonic units according to Handy et al. (2015).

direction during the model search. At the other locations, the fast axis are color coded according to whether the direction is poorly or well constrained. A high directional standard deviation can be due to different reasons. If the uncertainty in the anisotropy in the phase-velocity maps is large, this large uncertainty is propagated into the shear-velocity anisotropy and typically increases during the depth inversion step. Another reason can be that the phase-velocity anisotropy is actually well constrained but the directions at adjacent periods are incompatible so that no model can be found that fits all the observations. Finally, an approximately isotropic layer will also result

in no definable anisotropy and thus a high directional standard deviation. The combination of well constrained direction and isotropic average structure (e.g. Figure 7 at 5 km, 47.5°N) occurs when the majority of models produced by the model search are isotropic but those models that include anisotropy have a clear preferential fast axis direction.

The isotropic velocities in the maps at shallow depths are dominated by the contrast between the slow Molasse and Po basin, north and south of the Alps, and the fast shear velocities within the Alps. At middle crustal levels, at 20 km depth, lower velocities are imaged underneath the Alps, possibly due to the thickened and heated crust. At depths from 30 to 40 km, the low velocities under the Alps and Dinarides are due to the thick crust, whereas the velocities surrounding the mountain chains show velocities typical of the lowermost crust and uppermost mantle. At 50 km depth, the low velocities in the center of the map would correspond to either very high-velocity lowermost crustal material or relatively slow uppermost mantle. At this depth range there is also a considerable amount of vertical smearing, since we are not able to image sharp velocity contrasts such as the Moho (Figure 5f).

The azimuthal anisotropy shows a predominant E-W orientation at depths down to 20 km. Only few regions are well defined at the shallowest depth level. At 5–20 km depth, the well constrained region lies around the Periadriatic fault zone and in parts of the southern Alps. At greater depths, the fast axis orientation changes dramatically under the Alps, showing a N-S orientation, most prominent west of the Giudicarie fault and east of the Tauern window. In the northern Alpine foreland a clear arc-parallel pattern of fast-axis orientations can be observed. The two-layer structure in the anisotropy can be seen also in the profiles (Figure 8). In many sections, there is an orogen-parallel anisotropy in the upper crustal part, approximately down to the 3.6 km/s iso-velocity contour. The lower, orogen-perpendicular anisotropy under the Alps is concentrated in the bottom half of the crust and partially extends into the uppermost mantle. In the profiles, the Moho depth is approximated by the 4.15 km/s iso-velocity contour, since it was made a requisite of the depth inversion that only models that show a velocity jump between 4.1 km/s and 4.2 km/s are accepted. In the supplement, the reader will find two alternative models, one that is obtained from removing the restrictions on the Moho boundary and on the gradient between adjacent layers (Figures S15–S17 in Supporting Information S1) and another one that includes more layers (Figures S18–S20 in Supporting Information S1).

5. Discussion

5.1. Anisotropic Depth Resolution

The results for most parts of the map show one or two anisotropic layers and for many profiles these layers coincide with the isotropic layering of upper and lower crust. We test whether it is possible to resolve more than two layers with the applied method by conducting a series of synthetic tests. Several models with four isotropic layers (sediments, upper crust, lower crust, mantle) and different anisotropic layering are set up for which we generate synthetic dispersion curves. There is no error added to the synthetic data, but the standard deviations of the input data $\sigma_{(0,1,2)}$ are chosen based on the average, measured uncertainties and is fixed during the model search. The test in Figure 9 includes anisotropic layers that do not exactly coincide with the isotropic layers. The recovered model shows that the anisotropic directions in the sedimentary layer and in the upper crustal layer are well resolved. There is a reduction of the anisotropic amplitudes at around 20 km where the input model is isotropic. The lower crustal and the uppermost mantle layers are not clearly distinguishable as two separate anisotropic layers in the recovered model. Additionally, in the upper mantle, the amplitudes fade quickly which relates to the lower resolution at long periods, as evidenced by the sensitivity kernels (Figure S1 in Supporting Information S1), and the relatively large data uncertainty. All of the recovered mean amplitudes are smaller than the input anisotropic amplitudes, which is due to averaging models with different fast-axis directions. More synthetic test are shown in the supplement to this article (Figures S7–S11 in Supporting Information S1). From the tests we find that the anisotropy is potentially not well resolved in the lower crust and uppermost mantle. A situation as depicted in the real-data example in Figure 5, with similar anisotropic amplitudes and different directions in the upper and lower crust, may either be caused by a very strong anisotropy in the lower crust (10% input anisotropy results in ~5% recovered anisotropy), or a similar anisotropic fast-axis direction in the lower crust and the uppermost mantle. We also find that an anisotropic layer of 10 km or less at depths greater 20 km is probably not resolvable with our data. To improve the resolution, especially in the deeper parts of the model, significantly reduced data uncertainties would be necessary (Figure S11 in Supporting Information S1).
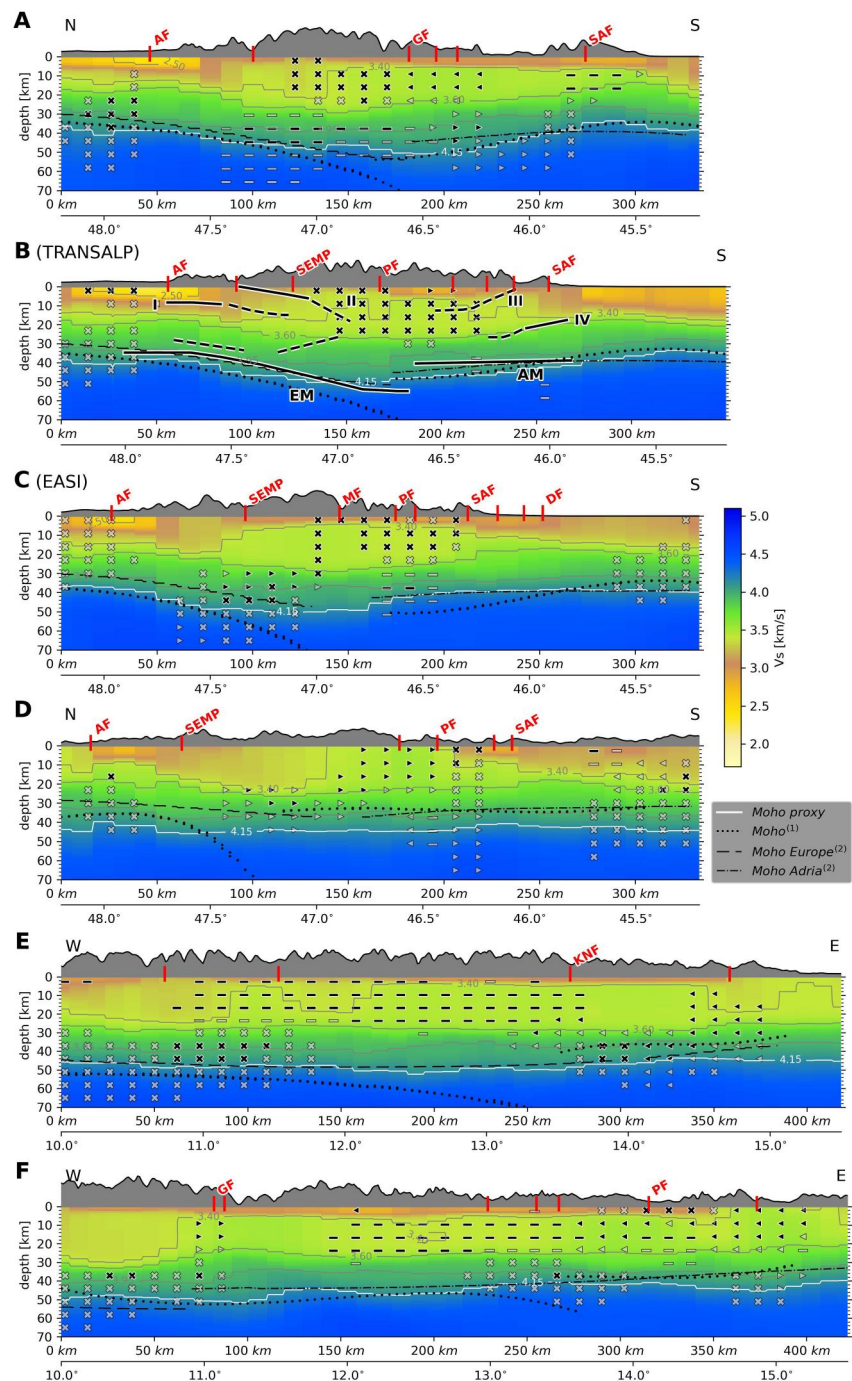
Figure 8. Cross-section along the traces shown in Figure 7. The red markers and labels at the surface correspond to the lineaments in Figure 1. The 4.15 km/s velocity contour is taken as Moho proxy and compared to the Moho estimates of [1]Mroczek et al. (2023) and [2]Spada et al. (2013). The black and gray markers in the sections indicate the fast-axis direction of the azimuthal anisotropy with the same color coding as in Figure 7. A line marker indicates that the fast axis is parallel within ±30° from the strike of the section, a cross means that it is perpendicular in the ±30° range. Triangles indicate oblique fast axis, where triangles pointing to the right indicate fast axis pointing in positive x-direction and away from the viewer and triangles pointing to the left indicate fast axis pointing in positive x-direction and toward the viewer. No marker is drawn where the uncertainty of the anisotropy is too large, identical to Figure 7. Areas with high velocity standard deviation (≥0.2 km/s) are shown in muted colors.
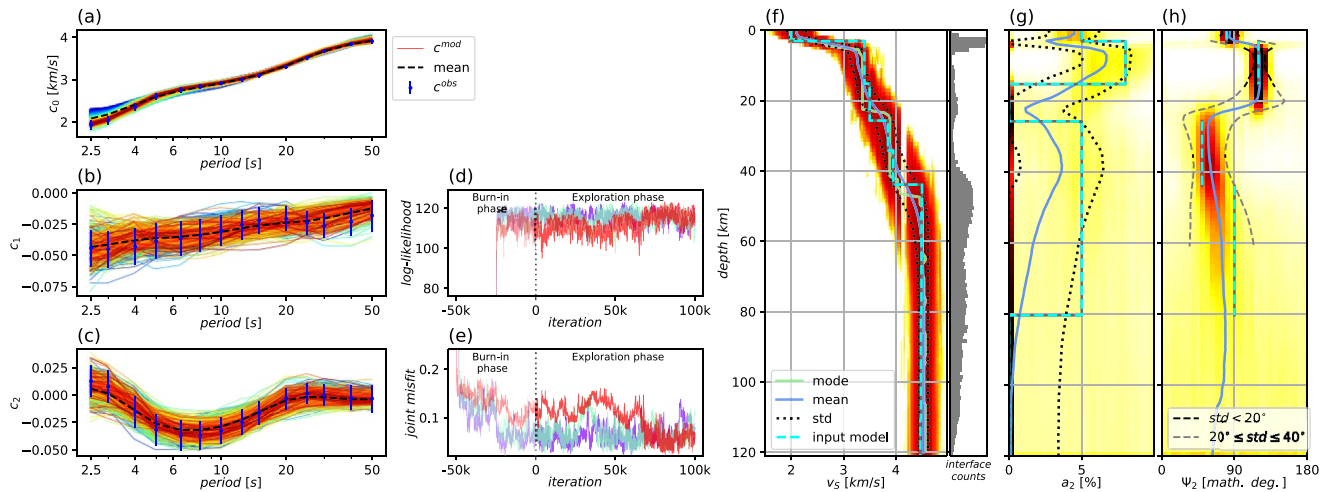
Figure 9. Synthetic example for a depth model with four isotropic and four anisotropic layers that only approximately coincide. The dashed cyan lines show the isotropic and anisotropic input model. The recovered model and the data fit is presented in the same way as in Figure 5. The input values of c_0, c_1, and c_2 are not perturbed with random errors but their uncertainties are fixed at values typical for those obtained from the real data.

Moreover, it was shown by Bodin et al. (2016) that adding more data types such as body waves leads to much better constrained anisotropic amplitudes and directions.

5.2. Isotropic Crustal Structure

Most of the major velocity contrasts close to the surface approximately follow geologic structures, such as the southern limit of the northern Alpine Molasse basin, the high velocities in the Bohemian massif at the northern edge of our study region or the limit between the southern Alps and the post-Miocene sedimentary cover south of it (Figure 7). The highest velocities in the eastern Alps are found just north of the Periadriatic line while the fast velocities are less pronounced in the southern Alps. This difference has also been observed by Molinari et al. (2020) who attribute the slightly lower velocities in the southern Alps to the limestone-calcareous rocks. The sedimentary thickness can be estimated based on the interface probability shown in Figure S14 of the Supporting Information S1 in conjunction with the low velocities as seen in the profiles in Figure 8. The interface probabilities are calculated from the interface counts as shown in Figure 9f, weighted by the vertical gradient of the mean v_S profile. The results indicate a thick sedimentary basin north of the Alps that deepens from ~4 km in the north to a maximum depth of 6 km (Figure 8). This is in good agreement with the surface-wave study of Molinari et al. (2020), a bit thicker than the estimate of Bigi et al. (1990) of 4.5 km and slightly shallower than the depth of the reflector **I** from the active seismic experiment reported by Lüschen et al. (2004) in profile B (Figure 8). The southern limit of the low-velocity basin is offset to the south from the Alpine frontal thrust which may be due to the southward dip of the fault that emplaced Mesozoic units of the northern calcareous Alps on top of the Molasse sediments (e.g., Schmid et al., 2004). South of the southern Alpine front, the model shows a velocity interface deepening from 6 to 14 km toward the Adriatic sea. The observed velocities close to the surface are around 2.5–2.8 km/s and thus higher than the ones observed in the northern Alpine Molasse basin and the Po basin (Figure 8). This is in agreement with the much thinner (1–2 km) sedimentary cover in the Friuli plain as compared to the Molasse and Po basin depths; the velocity interface at an average depth of 10 km would therefore correspond to the depth of the mostly Mesozoic carbonate units that outcrop north of the southern Alpine front (e.g., Fantoni & Franciosi, 2010).

Outside the sedimentary basins, the shear velocities close to the surface are typically around 3.0 km/s with a faster velocity increase with depth underneath the Alps compared to the forelands. The highest velocities close to the surface are imaged under the western part of the Tauern window (profile B), the central part of profile D and in the southern central Alps (Figure 7), similar to the distribution of shallow, fast structures imaged by Qorbani et al. (2020). These very fast velocities may be due to crustal stacking and exhumation of basement rocks, even though it is unclear why the shallowest structures should be faster in the western part of the Tauern window compared to its eastern part, as already pointed out by Qorbani et al. (2020).

The upper crustal velocity is relatively constant in most parts of the map at around 3.5 km/s. In some profiles, we find a velocity reduction within the upper crust, for example, in profile B at around 46.5°. This coincides roughly with the interface labeled **III** interpreted from the active seismic Transalp experiment who attribute this to a major thrust fault termed Sub-Dolomites Ramp, where lower crustal material may be placed on top of upper crustal units (Lüschen et al., 2004). A detailed inspection shows, however, that a weak negative velocity gradient is found almost everywhere within the upper crust under the Alps. Thus, it might alternatively indicate a temperature increase due to crustal stacking. An inverse velocity gradient in this depth range is also found by Qorbani et al. (2020) and Sadeghi-Bagherabadi et al. (2021), at around 20 km depth under the Alps in many of their profiles. The latter note that there is a coincidence of the typical earthquake depth in this region with the high-velocity layer between about 3 and 15 km depth with only few earthquakes localized in the low-velocity layer underneath.

Upper and lower crust are separated by a velocity jump close to the 3.6 km/s iso-velocity contour. This interface is typical also for regional and global reference crustal models (e.g., PREM, EPCrust, Dziewonski & Anderson, 1981; Molinari & Morelli, 2011). Models generated by the rj-McMC algorithm are naturally parsimonious so that fewer layers are preferred if they are able to explain the data equally well as those models with more layers (Bodin et al., 2016). This often results in a 3-layer crustal structure for the individual models and might thus favor a velocity jump around 3.6 km/s while the true velocity increase is more gradual. We perform a test where we prescribe a minimum number of 10 layers for each model search so that more complex crustal models are encouraged (Figures S18–S20 in Supporting Information S1). As expected, the velocity increase within the crust is smoother when forcing more layers, nevertheless the strongest positive velocity contrast below the sediments is still found at around 3.6 km/s which supports the idea of a separation between upper and lower crust at approximately this velocity contour (Figure S20 in Supporting Information S1).

Jozi Najafabadi et al. (2022) make use of local earthquakes to image the crustal structure in approximately the same region as this study. They define the lower crust as a layer between the Moho and the $v_P = 6.8$ km/s contour which translates approximately into $v_S = 3.95$ km/s, shown in the profiles in Figure 8. In the following, this will be termed the lowermost crust. Their model indicates the existence of a thickened lowermost crust which they interpret to represent a stack of Adriatic lower crust that forms the tip of the Adriatic indenter (Jozi Najafabadi et al., 2022). The herein presented surface-wave model shows a similar "bulge" in the 3.95 km/s contour in profile B on top of the Adriatic Moho and in profile C underneath the Tauern window. This means that the structure is located further to the south along the Transalp profile compared to Jozi Najafabadi et al. (2022), but it would still be compatible with their interpretation of a thickened lowermost Adriatic crust. As pointed out by Jozi Najafabadi et al. (2022) this is not the only possible interpretation since there is no clear evidence of the origin of this bulge (European vs. Adriatic vs. a combination). The existence of this lowermost crustal bulge is further uncertain in our surface-wave model: In the less restricted model shown in the supplement (Figure S16 in Supporting Information S1), no thickening in the lowermost crust appears but rather a small bulge in the Moho. Again, this interpretation is dependent on the choice of the Moho proxy.

The shear-velocity maps in Figure 7 and the E-W section in Figure 8f show a clear velocity contrast that approximately coincides with the Giudicarie line, similar to previous studies (Lu et al., 2020; Sadeghi-Bagherabadi et al., 2021). At shallow depth (2 km) the contrast is weak with a tendency of faster velocities in the west. Between 10 and 30 km there is a clear contrast from slower velocities in the west to faster velocities in the east. We find that these faster velocities in the east are not representative of the entire southern Alps but rather mark a zone of approx. 60 km in E-W extension. The continuation of this structure below 30 km depth is unclear in our model, but there is a small offset in the Moho proxy contour (Figure 10). Sadeghi-Bagherabadi et al. (2021) report that there is an approximate spatial coincidence of the fast velocities with Permian magmatic rocks (Schuster & Stüwe, 2008) and suggest that it might indicate the depth continuation of this structure (compare also Figure S13 in Supporting Information S1). Also Lu et al. (2020) find an anomaly in the 4.1 km/s velocity contour in this region that they attribute to Permian magmatic rocks, though much smaller in scale.

5.3. Moho Structure

The Moho depth is approximated with the 4.15 km/s velocity contour, since the models are required to have a velocity jump around this velocity range as explained in Section 3. The proxy depth is greatest below the orogen going to more than 50 km depth, shallowing toward the east, and is around 32 km in the forelands (Figure 10). The
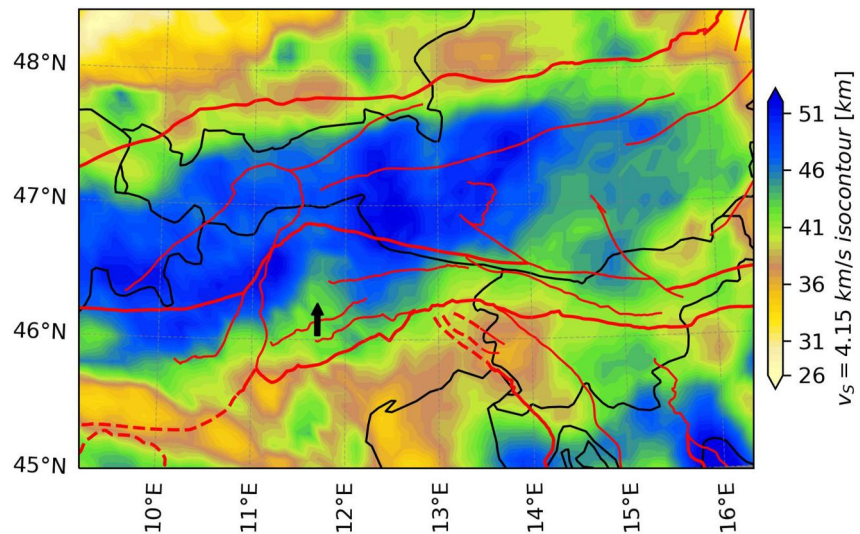
Figure 10. Depth of the 4.15 km/s iso-velocity contour in the mapped area which is taken as a proxy for the Moho depth. The arrow marks a region of thinned Moho depth east of the Giudicarie Fault (GF) discussed in the text. Red lineaments are the same as in Figure 1.

proxy depth corresponds also to the maximum interface probability as shown in Figure S14 of the Supporting Information S1. The Moho proxy is similar to previous estimates from receiver functions (Kummerow et al., 2004; Mroczek et al., 2023; Spada et al., 2013). The depth differences between this study and the inferred depths from Spada et al. (2013) and those from the receiver-function study of Mroczek et al. (2023) are mostly in the range of 0–10 km as can be seen from the profiles in Figure 8. This range is similar to the range of discrepancies between different receiver function studies. Since the Moho proxy from surface waves is relatively smooth, it is not possible to extract a reliable estimate of the subduction polarity.

To better understand the influence of the required velocity discontinuity at around 4.15 km/s, an alternative model is presented in the supplement to this article that is created without this requirement and where no restriction on the velocity contrasts between layers is imposed (Figures S15–S17 in Supporting Information S1). We find that the overall crustal velocity structure remains the same, even though there are more complexities in the crust and the 4.15 km/s contour is generally shallower. The velocity increase across the crust-mantle transition is more gradual which thus increases the uncertainty on the Moho depth. Clearly, in this case a velocity contour can only be a rough approximation of the true Moho depth. Nevertheless, such a gradual increase or a small velocity contrast across the Moho is not unlikely in a plate convergence setting. It has been shown that eclogite-facies crustal rocks can have a shear velocity basically indistinguishable from uppermost mantle peridotite (e.g., ~4.6 km/s in Worthington et al. (2013)) which can be a problem when trying to detect the crust-mantle boundary, especially in regions of thickened crust (Wittlinger et al., 2009; Zertani et al., 2019). In combination with the low sensitivity of the dispersion curve inversion to velocity contrasts, this can explain the smooth gradual increase in shear velocities across the Moho. While the 4.15 km/s contour may be an appropriate proxy for a standard crust (e.g., Dziewonski & Anderson, 1981), a higher velocity might be more appropriate for the thickened crust under the orogen. This assumption is supported by the larger discrepancies between the receiver function Moho and the 4.15 km/s proxy close to the Europe-Adria plate interface, where the crust is thickest (45 km vs. 55–60 km in profile B in Figure 8). In the model where a Moho jump is required (Figure 8), the largest velocity contrast automatically coincides with the 4.15 km/s velocity contour. The deeper Moho close to the Europe-Adria plate interface fits better with the receiver function results in this case. The Moho depth estimate may, however, be biased wherever the crustal rock velocities are larger than 4.1 km/s so that our requirement of having a velocity interface between $v_S \leq 4.1$ and $v_S \geq 4.2$ is inappropriate. Nevertheless, we prefer the model with a required Moho discontinuity since it facilitates the estimation of the crustal thickness and since we know from receiver functions that there is a velocity discontinuity across the crust-mantle boundary for most parts of the study region (a possible exception may be the "Moho gap" in Spada et al. (2013) but with denser station coverage a Moho can apparently be imaged even in this area (Mroczek et al., 2023)).

The thickest crustal root with depths larger than ~45 km (blue region in Figure 10) is approximately delimited to the south by the Periadriatic Fault and Giudicarie Fault; the northern limit tracks the AF but is offset to the south by about 50 km. This implies a marked shift to the north when going from the central to the eastern Alps; the two deepest Moho depressions are separated by a strip of slightly reduced crustal thickness east of the Giudicarie Fault. This reduction in Moho depth is also seen in similar surface-wave studies (Kästle et al., 2018; Sadeghi-Bagherabadi et al., 2021); however, several other studies do not show such separation of the central and eastern Alpine Mohos (e.g., Diehl et al., 2009; Lu et al., 2020; Molinari & Morelli, 2011; Spada et al., 2013). The slightly reduced crustal thickness east of the Giudicarie Fault may thus simply be an artifact from using a velocity contour as Moho proxy. Nevertheless, there is an interesting coincidence between the depth of the Moho proxy in Figure 10 and the position of the slab anomalies in P-wave tomographic models that image a similar separation and northward offset between central and eastern Alpine slab anomalies (e.g., Hua et al., 2017; Koulakov et al., 2009; Lippitsch et al., 2003; Paffrath et al., 2021; Zhao et al., 2016). A possible scenario may thus be the underthrusting of crustal slivers that are being dragged by laterally discontinuous segments of the sinking Alpine slab. Alternatively, it may be related to crustal deformation resulting from the collision with Adria, since the location of the anomaly coincides spatially with the proposed tip of the Adriatic indenter (e.g., Handy et al., 2015). Sadeghi-Bagherabadi et al. (2021) offer a different interpretation and suggest that it might indicate the depth continuation of the above discussed structure linked to Permian magmatism.

5.4. Comparison to Previous Models of Azimuthal Anisotropy

A similar study of Kästle et al. (2022) shows anisotropic Rayleigh phase velocities for the entire Alpine region. The comparison to the herein presented results shows that the general structures are identical in the well resolved parts of the model (Figure S12 in Supporting Information S1). Differences in the isotropic velocities include the size of the very low-velocity zones and some structures at the model boundaries. The anisotropic fast axes differ mostly around regions of strong velocity contrasts. The Eikonal tomography method is very sensitive to errors in the reconstruction of the travel time field, which may explain differences where the structural contrasts are large. The fact that we can only account for the 2Ψ anisotropy in this study as opposed to 1Ψ, 2Ψ, and 4Ψ variations in Kästle et al. (2022) may be another reason for some discrepancies.

The study of Fry et al. (2010) images the azimuthal anisotropy with ambient noise in Switzerland which partially overlaps with our study region. They find a similar trend of E-W anisotropy in the eastern part of their model that rotates toward a N-S direction with increasing period. A discrepancy between the models is only found at around 35 s period where they report a N-S trend of the anisotropic fast axis both within the Alps and in the northern foreland, whereas our results exhibit E-W fast directions in the foreland (in accordance with Kästle et al., 2022). The beamforming technique applied by Soergel et al. (2022) extracts the propagation azimuths directly from the observed travel-time field, similar to the Eikonal method. They compare their phase-velocity anisotropy to the results of Kästle et al. (2022) and find generally good agreement with the largest discrepancies again found close to the model borders and in regions of strong velocity contrasts. Soergel et al. (2022) provide the only other study that inverts the anisotropic phase velocities to azimuthal shear-velocity anisotropy in the Alpine crust. Due to the lower resolution that is inherent to their method, they can only image the average depth structure at some selected points in the Alps. As in our work, they find a predominant E-W orientation of the fast axis in the upper crust and a change to a N-S orientation in the lower crust in the central Alps. The lower crustal orientations for the eastern Alps are not compatible between the studies, even though a similar trend is observable from an E-W orientation toward a N-S orientation from upper crust to uppermost mantle. This may be related to the lower resolution of our approach in the lower crust and the uppermost mantle since we fix the data uncertainties at the values extracted from the phase-velocity maps. Soergel et al. (2022) maintain the relative uncertainty difference between measurements at different periods, but let the algorithm choose the absolute value of the uncertainty. This means that when the data is well-behaved, they fit their anisotropic c_1 and c_2 measurements much closer, giving a "better" resolution at depth. We, however, prefer to use the measured uncertainties as discussed in Section 5.1.

Schippkus et al. (2020) study the azimuthal group-velocity anisotropy in the Vienna basin which is at the northeasternmost limit of our study region. They find a good agreement of their N-S/NE-SW oriented fast-axis directions with the principal stress orientation and suggest that the short-period anisotropy is dominated by microcracks aligned with the maximum stress (see Section 2). The fast-axis orientations in Figure 6 are somewhat similar to those imaged by Schippkus et al. (2020), but do not show this approximate N-S orientation further away from the Vienna basin. We find that at short periods, the dominant orientation in the eastern Alps is orogen-

parallel for the phase-velocity maps (Figure 6), as well as in the shear-velocity maps (Figure 7). The large-scale stress field is mostly N-S oriented in the eastern Alps and only rotates in an E-W direction toward the Pannonian basin (Heidbach et al., 2016). This means that on the larger scale, we find no simple relation between the stress field and the anisotropy at 2–5 km depth, as already stated by Kästle et al. (2022). Schippkus et al. (2020) point out that faults may influence the stress field locally which may explain part of the mismatch between principal stress and fast axis orientations. It is also possible that due to the lack of very short period data, we are not able to see the stress-parallel anisotropy from shallow microcracks in our model.

5.5. Layered Anisotropic Structure

The orogen parallel orientation in almost the entire upper Alpine crust may be explained by an alignment of structures due to the Cenozoic compression. This includes E-W oriented foliation (e.g., Rosenberg et al., 2018, and references therein) as well as folding and thrusting due to N-S compression causing E-W oriented structures that lead to SPO anisotropy. The SPO may be enhanced by intrinsic anisotropy due to minerals aligning parallel to the foliation such as highly anisotropic micas (e.g., Fry et al., 2010; Keppler et al., 2021). Nevertheless, also this concept does not provide a fully coherent picture when looking at the curvature of the fast anisotropic axis around the Giudicarie fault. This structure is related to a sinistral strike-slip movement due to the indentation of Adria (e.g., Scharf et al., 2013), which, however, would not necessarily rotate the pre-existing foliation or fold structures to a fault-parallel orientation. The fault-parallelism of the upper crustal anisotropy in the Alps is one of the main findings of this study and also in general agreement with the mapped fast axis in Schippkus et al. (2020) and Soergel et al. (2022). Even in SKS splitting results, there are indications for a fault-parallelism around the Giudicarie zone (e.g., Link & Rümpker, 2021). A possible mechanism might be differential material movement both laterally and vertically around the faults that leads to a strain-parallel mineral orientation, similarly suggested by Schippkus et al. (2020). Unfortunately, with the currently available information it is not possible to go beyond speculations on the micro- or macroscopic mechanisms that are responsible for the observed fault-parallel anisotropy.

We find a spatial correlation between the areas with large seismic activity (Hofman et al., 2023; Serpelloni et al., 2016) and pronounced, shallow azimuthal anisotropy. This is most evident in the eastern southern Alps and toward the Alps-Dinarides transition. The area just east of the Giudicarie fault, characterized by elevated velocities in the middle crust, possibly representing the core of the Adriatic indenter, shows no clear anisotropy and correspondingly there is also very little seismic activity (Hofman et al., 2023). Nevertheless, there are also contradictory observations, such as the strong anisotropy along the Giudicarie fault and western Periadriatic fault, where seismic activity is low, as well as the absence of clear anisotropy in the western part of the southern Alpine front (Bassano fault zone) which does show seismic activity. The correlation may thus be rather related to cumulative (past and present) fault activity and the resulting amount of deformation.

In the lower crust, the fast-axis directions change dramatically under the central Alps, approximately pointing in N-S direction. Soergel et al. (2022) propose that this may be caused by late Carboniferous stretching that affected the entire region (Guillot et al., 2009) without any later, Alpine overprint. Fry et al. (2010) suggest that the lower European crust is uplifting in response to the retreating European slab. The associated crustal movement is proposed to have a vertical and a northward component that would explain the N-S oriented anisotropy. Our model shows N-S anisotropy almost exclusively north of the Periadriatic fault which may be an indication that it is indeed related to the subduction of the European plate. However, there are only few measurements south of the Periadriatic line that fulfill the quality criteria in the shear-velocity map (Figure 7). East of the Tauern window, where we have measurements at depth, the change is not as dramatic: The upper crustal NW-SE fast-axis orientations rotate further in NNW-SSE direction. Since this is roughly parallel to the central Alpine orientations, there may be similar mechanisms affecting the anisotropy in the entire lower Alpine crust.

A similar two layer crustal anisotropy has also been observed by Huang et al. (2015) in Taiwan, with an orogen parallel orientation down to ∼15 km depth and an orogen perpendicular orientation below. They relate the upper crustal fast axis directions to collisional structures and the lower crustal ones to orogen-perpendicular shear due to the ongoing subduction. A two layer crustal anisotropy is found also by Fu et al. (2016) in northern China where, as in our study, the upper crustal anisotropy (10–16 s period) is oriented mostly parallel to the main fault structures and perpendicular in the lower crust (25 s). An interesting outcome from many of these (and other) works is the layered and relatively homogeneous pattern of seismic anisotropy within the same orogen/region (Agius &

Lebedev, 2017; Endrun et al., 2011; Fu et al., 2016; Guo et al., 2017; Huang et al., 2015; Xie et al., 2017). Several of these studies further report an upper crustal layer with anisotropic fast axes approximately parallel to the main structural trends and an opposite (90°) orientation is in the lower layer (lower crust and or uppermost mantle). The transition depth ranges from 10 to 30 km. This is deeper than the expected brittle-ductile transition for a typical crustal setting (Kern & Schmidt, 1990), but possible mechanisms include decoupling between upper and lower crust, changes in the mineral assemblage and in the rheology.

The anisotropy in the eastern Alps may be affected by the eastward extrusion with associated stretching of ∼26 km in the western Tauern window and ∼70 km in the western Tauern window according to Scharf et al. (2013). The E-W oriented anisotropy can be followed to almost 30 km in our model (Figure 8). This could point to a detachment between upper and lower crust at this depth. However, since the E-W directed anisotropy is not well confined to the region of known eastward extrusion, between the Periadriatic Fault and the SEMP faults, there are probably other, more important dynamics as the ones mentioned above that control the anisotropy in this region.

In the northern Alpine foreland, the model shows a very homogeneous pattern of anisotropies that follow the Alpine arc from intermediate crustal depths into the uppermost mantle. Similar directions are found by Soergel et al. (2022) north of the Alps. This is very similar to the pattern of anisotropies from SKS splitting which are, however, mostly attributed to LPO of minerals in the asthenosphere (e.g., Barruol et al., 2011; Kummerow & Kind, 2006), although more complex interpretations involving various mechanism are also sometimes invoked (Löberich & Bokelmann, 2022; Qorbani et al., 2015). Fry et al. (2010) propose a Variscian origin of the crustal anisotropy in the northern foreland. This may indicate that the same processes has affected the entire lithosphere in the foreland and potentially even the asthenosphere. Agius and Lebedev (2017) infer that a major part of the observed SKS splitting times are actually accumulated in the crust for their model. Given the parallel distribution of fast-axis orientations in our model and in SKS splitting results (e.g., Petrescu et al., 2020; Wüstefeld et al., 2009), we think this also is a plausible assumption for the northern Alpine foreland. Within the Alpine crust, in turn, the two layers of anisotropy with perpendicular fast directions are expected to nearly cancel out in SKS measurements, so that published SKS results are more likely to show mantle anisotropy for this region.

6. Conclusions

This work shows how data from a very dense, regional seismic network can be used to extract Rayleigh phase travel times that are inverted with a two-step rj-McMC approach for an azimuthally anisotropic shear-velocity model of the crust. We propagate the uncertainties obtained from the phase-velocity maps into the depth inversion to make sure that we do not overfit our data, which can otherwise be a problem in such a two-step approach. In general, we find good agreement between our work and previous studies, but is the first time that the shear-velocity anisotropy is resolved in this detail (10 km spaced grid) in the eastern Alpine crust. The synthetic tests suggest that the anisotropy in the upper half of the crust is well resolved, while below, complex anisotropic patterns would tend to cancel out and the vertical resolution makes it difficult to distinguish between lower crustal and uppermost mantle anisotropy. We find that our model results are stable with respect to different setups of the model search and conclude that there is only a small tradeoff between the isotropic velocity structure and the imaged anisotropic fast axis.

A zone of high velocities and a small offset in the Moho depth east of the Guidicarie fault may be related to Permian magmatic rocks, as proposed in previous works. However, we notice that this separation also spatially coincides with different segments of the deeper slab anomalies in mantle tomographic models. We only find weak indications of the lowermost crustal thickening related to the indentation of the Adriatic plate which was proposed by Jozi Najafabadi et al. (2022).

The anisotropic model suggests a two layer structure of azimuthal anisotropy under the Alps, where the upper layer is approximately orogen parallel and follows major fault lines. Below ∼20 km depth, the fast axis are more orogen perpendicular oriented. This could indicate a detachment between upper and lower crust or differences in the rheology. Future studies will profit from including different data sources (Love waves, receiver functions) to be able to resolve more of the elastic tensor and better deal with ambiguities. The rj-McMC method is a promising approach to do so, since it is relatively straightforward to combine different data sets, each with their individual data uncertainties and allowing to consequently propagate measurement errors. This is necessary to link

petrological laboratory measurements to the effective seismic anisotropy and help to decipher the geodynamic processes that lead to large-scale anisotropy.

Data Availability Statement

The Python scripts used in this study are available from Kästle and Tilmann (2023a), Kästle and Tilmann (2023b), and Kästle and Tilmann (2023c). The data from the AlpArray experiment is distributed through ORFEUS and EIDA (www.orfeus-eu.org/data/eida/). The AlpArray Seismic Network comprises the temporary AlpArray stations (AlpArray Seismic Network, 2015), SWATH-D stations (Heit et al., 2017) and the following permanent networks: BW (University of München, 2001), CH (Swiss Seismological Service, ETH Zurich, 1983), CR (University of Zagreb, 2001), FR (RESIF, 1995), HU (Kövesligethy Radó Seismological Observatory, 1992), G (Institut de physique du globe de Paris (IPGP) & École et Observatoires des Sciences de la Terre de Strasbourg (EOST), 1982), GE (GEOFON Data Centre, 1993), GR (Federal Institute for Geosciences & Natural Resources, 1976), GU (University of Genoa, 1967), HS (Hessian Agency for Nature Conservation & Geology, 2012), IU (Albuquerque Seismological Laboratory/USGS, 2014), NI (OGS (Istituto Nazionale di Oceanografia e di Geofisica Sperimentale) & University of Trieste, 2002), OE (ZAMG—Zentralanstalt für Meterologie und Geodynamik, 1987), OX (Istituto Nazionale di Oceanografia e di Geofisica Sperimentale— OGS, 2016), RD (RESIF, 2018), RF (University of Trieste, 1993), SK (ESI SAS; Former GPI SAS (Geophysical Institute Of The Slovak Academy Of Sciences), 2004), SL (Slovenian Environment Agency, 1990), ST (Geological Survey-Provincia Autonoma di Trento, 1981), SX (University of Leipzig, 2001), TH (Friedrich-Schiller-Universitaet Jena, 2009).

References

Agius, M. R., & Lebedev, S. (2017). Complex, multilayered azimuthal anisotropy beneath Tibet: Evidence for co-existing channel flow and pure-shear crustal thickening. *Geophysical Journal International*, *210*(3), 1823–1844. https://doi.org/10.1093/gji/ggx266

Aki, K. (1957). Space and time spectra of stationary stochastic waves, with special reference to microtremors. *Bulletin of the Earthquake Research Institute, University of Tokyo*, *35*(3), 415–456.

Albuquerque Seismological Laboratory/USGS. (2014). Global seismograph network (GSN—IRIS/USGS) [Dataset]. *International Federation of Digital Seismograph Networks*. https://doi.org/10.7914/SN/IU

Alder, C., Bodin, T., Ricard, Y., Capdeville, Y., Debayle, E., & Montagner, J. (2017). Quantifying seismic anisotropy induced by small-scale chemical heterogeneities. *Geophysical Journal International*, *211*(3), 1585–1600. https://doi.org/10.1093/gji/ggx389

Alder, C., Debayle, E., Bodin, T., Paul, A., Stehly, L., Pedersen, H., & the AlpArray Working Group. (2021). Evidence for radial anisotropy in the lower crust of the Apennines from Bayesian ambient noise tomography in Europe. *Geophysical Journal International*, *226*(2), 941–967. https://doi.org/10.1093/gji/ggab066

Almqvist, B. S., & Mainprice, D. (2017). Seismic properties and anisotropy of the continental crust: Predictions based on mineral texture and rock microstructure. *Reviews of Geophysics*, *55*(2), 367–433. https://doi.org/10.1002/2016rg000552

AlpArray Seismic Network. (2015). AlpArray seismic network (AASN) temporary component [Dataset]. https://doi.org/10.12686/ALPARRAY/Z3_2015

Backus, G. E. (1962). Long-wave elastic anisotropy produced by horizontal layering. *Journal of Geophysical Research*, *67*(11), 4427–4441. https://doi.org/10.1029/jz067i011p04427

Barruol, G., Bonnin, M., Pedersen, H., Bokelmann, G. H., & Tiberi, C. (2011). Belt-parallel mantle flow beneath a halted continental collision: The Western Alps. *Earth and Planetary Science Letters*, *302*(3–4), 429–438. https://doi.org/10.1016/j.epsl.2010.12.040

Barruol, G., & Mainprice, D. (1993). 3-D seismic velocities calculated from lattice-preferred orientation and reflectivity of a lower crustal section: Examples of the Val Sesia section (Ivrea zone, northern Italy). *Geophysical Journal International*, *115*(3), 1169–1188. https://doi.org/10.1111/j.1365-246x.1993.tb01519.x

Bennett, L., Melchers, B., & Proppe, B. (2020). *Curta: A general-purpose high-performance computer at ZEDAT*. Freie Universität Berlin. https://doi.org/10.17169/refubium-26754

Berteussen, K.-A. (1977). Moho depth determinations based on spectral-ratio analysis of NORSAR long-period P waves. *Physics of the Earth and Planetary Interiors*, *15*(1), 13–27. https://doi.org/10.1016/0031-9201(77)90006-1

Beyreuther, M., Barsch, R., Krischer, L., Megies, T., Behr, Y., & Wassermann, J. (2010). ObsPy: A Python toolbox for seismology. *Seismological Research Letters*, *81*(3), 530–533. https://doi.org/10.1785/gssrl.81.3.530

Bigi, G., Cosentino, D., Parotto, M., Sartori, R., & Scandone, P. (1990). Structural model of Italy, 1:500.000. *Quaderni de La Ricerca Scientifica, C.N.R.*, *114*(3).

Bodin, T., Leiva, J., Romanowicz, B., Maupin, V., & Yuan, H. (2016). Imaging anisotropic layering with Bayesian inversion of multiple data types. *Geophysical Journal International*, *206*(1), 605–629. https://doi.org/10.1093/gji/ggw124

Bodin, T., & Sambridge, M. (2009). Seismic tomography with the reversible jump algorithm. *Geophysical Journal International*, *178*(3), 1411–1436. https://doi.org/10.1111/j.1365-246x.2009.04226.x

Bodin, T., Sambridge, M., Tkalčić, H., Arroucau, P., Gallagher, K., & Rawlinson, N. (2012). Transdimensional inversion of receiver functions and surface wave dispersion. *Journal of Geophysical Research*, *117*(B2), B02301. https://doi.org/10.1029/2011jb008560

Brownlee, S. J., Schulte-Pelkum, V., Raju, A., Mahan, K., Condit, C., & Orlandini, O. F. (2017). Characteristics of deep crustal seismic anisotropy from a compilation of rock elasticity tensors and their expression in receiver functions. *Tectonics*, *36*(9), 1835–1857. https://doi.org/10.1002/2017tc004625

Carminati, E., Lustrino, M., & Doglioni, C. (2012). Geodynamic evolution of the central and western Mediterranean: Tectonics vs. igneous petrology constraints. *Tectonophysics*, *579*, 173–192. https://doi.org/10.1016/j.tecto.2012.01.026

Chen, Y., Chen, Y., Fomel, S., Savvaidis, A., Saad, O. M., & Oboué, Y. A. S. I. (2023). Pyekfmm: A Python package for 3D fast-marching-based traveltime calculation and its applications in seismology. *Seismological Research Letters*, *94*(1), 2050–2059. https://doi.org/10.1785/0220230042

Crameri, F. (2018). Scientific color maps. https://doi.org/10.5281/zenodo.1243862

Crampin, S. (1994). The fracture criticality of crustal rocks. *Geophysical Journal International*, *118*(2), 428–438. https://doi.org/10.1111/j.1365-246x.1994.tb03974.x

Diehl, T., Husen, S., Kissling, E., & Deichmann, N. (2009). High-resolution 3-D P-wave model of the Alpine crust. *Geophysical Journal International*, *179*(2), 1133–1147. https://doi.org/10.1111/j.1365-246x.2009.04331.x

Dosso, S. E., Dettmer, J., Steininger, G., & Holland, C. W. (2014). Efficient trans-dimensional Bayesian inversion for geoacoustic profile estimation. *Inverse Problems*, *30*(11), 114018. https://doi.org/10.1088/0266-5611/30/11/114018

Dreiling, J., & Tilmann, F. (2019). BayHunter-McMC transdimensional Bayesian inversion of receiver functions and surface wave dispersion. *GFZ Data Services*. https://doi.org/10.5880/GFZ.2.4.2019.001

Dziewonski, A. M., & Anderson, D. L. (1981). Preliminary reference Earth model. *Physics of the Earth and Planetary Interiors*, *25*(4), 297–356. https://doi.org/10.1016/0031-9201(81)90046-7

Ekström, G., Abers, G. A., & Webb, S. C. (2009). Determination of surface-wave phase velocities across USArray from noise and Aki's spectral formulation. *Geophysical Research Letters*, *36*(18), L18301. https://doi.org/10.1029/2009gl039131

Endrun, B., Lebedev, S., Meier, T., Tirel, C., & Friederich, W. (2011). Complex layered deformation within the Aegean crust and mantle revealed by seismic anisotropy. *Nature Geoscience*, *4*(3), 203–207. https://doi.org/10.1038/ngeo1065

Erdman, M. E., Hacker, B. R., Zandt, G., & Seward, G. (2013). Seismic anisotropy of the crust: Electron-backscatter diffraction measurements from the basin and range. *Geophysical Journal International*, *195*(2), 1211–1229. https://doi.org/10.1093/gji/ggt287

ESI SAS; Former GPI SAS (Geophysical Institute Of The Slovak Academy Of Sciences). (2004). National network of seismic stations of Slovakia [Dataset]. *GFZ Data Services*. https://doi.org/10.14470/FX099882

Fantoni, R., & Franciosi, R. (2010). Tectono-sedimentary setting of the Po Plain and Adriatic foreland. *Rendiconti Lincei*, *21*(1), 197–209. https://doi.org/10.1007/s12210-010-0102-4

Federal Institute for Geosciences, & Natural Resources. (1976). German regional seismic network (GRSN) [Dataset]. https://doi.org/10.25928/MBX6-HR74

Fichtner, A., Kennett, B. L., & Trampert, J. (2013). Separating intrinsic and apparent anisotropy. *Physics of the Earth and Planetary Interiors*, *219*, 11–20. https://doi.org/10.1016/j.pepi.2013.03.006

Friedrich-Schiller-Universitaet Jena, I. f. G. (2009). Thüringer Seismologisches Netz [Dataset]. *International Federation of Digital Seismograph Networks*. https://doi.org/10.7914/SN/TH

Fry, B., Deschamps, F., Kissling, E., Stehly, L., & Giardini, D. (2010). Layered azimuthal anisotropy of Rayleigh wave phase velocities in the European Alpine lithosphere inferred from ambient noise. *Earth and Planetary Science Letters*, *297*(1–2), 95–102. https://doi.org/10.1016/j.epsl.2010.06.008

Fu, Y. V., Gao, Y., Li, A., Lu, L., Shi, Y., & Zhang, Y. (2016). The anisotropic structure in the crust in the northern part of North China from ambient seismic noise tomography. *Geophysical Journal International*, *204*(3), 1649–1661. https://doi.org/10.1093/gji/ggv549

Gallego, A., Panning, M., Russo, R., Comte, D., Mocanu, V., Murdie, R., & Vandecar, J. (2011). Azimuthal anisotropy in the Chile Ridge subduction region retrieved from ambient noise. *Lithosphere*, *3*(6), 393–400. https://doi.org/10.1130/l139.1

Gelman, A., Carlin, J. B., Stern, H. S., & Rubin, D. B. (1995). *Bayesian data analysis*. Chapman and Hall/CRC.

GEOFON Data Centre. (1993). GEOFON seismic network [Dataset]. *Deutsches GeoForschungsZentrum GFZ*. https://doi.org/10.14470/TR560404

Geological Survey-Provincia Autonoma di Trento. (1981). Trentino seismic network [Dataset]. *International Federation of Digital Seismograph Networks*. https://doi.org/10.7914/SN/ST

Green, R. G., Sens-Schönfelder, C., Shapiro, N., Koulakov, I., Tilmann, F., Dreiling, J., et al. (2020). Magmatic and sedimentary structure beneath the Klyuchevskoy volcanic group, Kamchatka, from ambient noise tomography. *Journal of Geophysical Research: Solid Earth*, *125*(3), e2019JB018900. https://doi.org/10.1029/2019jb018900

Guillot, S., di Paola, S., Ménot, R.-P., Ledru, P., Spalla, M. I., Gosso, G., & Schwartz, S. (2009). Suture zones and importance of strike-slip faulting for Variscan geodynamic reconstructions of the External Crystalline Massifs of the Western Alps. *Bulletin de la Societe Geologique de France*, *180*(6), 483–500. https://doi.org/10.2113/gssgfbull.180.6.483

Guo, Z., Gao, X., Yao, H., & Wang, W. (2017). Depth variations of azimuthal anisotropy beneath the Tian Shan Mt range (NW China) from ambient noise tomography. *Journal of Asian Earth Sciences*, *138*, 161–172. https://doi.org/10.1016/j.jseaes.2016.12.040

Handy, M. R., Schmid, S. M., Bousquet, R., Kissling, E., & Bernoulli, D. (2010). Reconciling plate-tectonic reconstructions of Alpine Tethys with the geological–geophysical record of spreading and subduction in the Alps. *Earth-Science Reviews*, *102*(3–4), 121–158. https://doi.org/10.1016/j.earscirev.2010.06.002

Handy, M. R., Ustaszewski, K., & Kissling, E. (2015). Reconstructing the Alps–Carpathians–Dinarides as a key to understanding switches in subduction polarity, slab gaps and surface motion. *International Journal of Earth Sciences*, *104*(1), 1–26. https://doi.org/10.1007/s00531-014-1060-3

Heidbach, O., Rajabi, M., Reiter, K., Ziegler, M., & the WSM Team. (2016). World stress map database release 2016. *GFZ Data Services*. https://doi.org/10.5880/WSM.2016.001

Heit, B., Cristiano, L., Haberland, C., Tilmann, F., Pesaresi, D., Jia, Y., et al. (2021). The SWATH-D seismological network in the Eastern Alps. *Seismological Society of America*, *92*(3), 1592–1609. https://doi.org/10.1785/0220200377

Heit, B., Weber, M., Tilmann, F., Haberland, C., Jia, Y., Carraro, C., et al. (2017). The Swath-D seismic network in Italy and Austria [Dataset]. *GFZ Data Services*. https://doi.org/10.14470/MF7562601148

Hessian Agency for Nature Conservation, E., & Geology. (2012). Hessischer Erdbebendienst [Dataset]. *International Federation of Digital Seismograph Networks*. https://doi.org/10.7914/SN/HS

Hetényi, G., Molinari, I., Clinton, J., Bokelmann, G., Bondár, I., Crawford, W. C., et al. (2018). The AlpArray seismic network: A large-scale European experiment to image the Alpine orogen. *Surveys in Geophysics*, *39*(5), 1009–1033. https://doi.org/10.1007/s10712-018-9472-4

Hofman, L. J., Kummerow, J., & Cesca, S. (2023). A new seismicity catalogue of the Eastern Alps using the temporary Swath-D network. *EGUsphere*, *14*(10), 1–32. https://doi.org/10.5194/se-14-1053-2023

Hua, Y., Zhao, D., & Xu, Y. (2017). P wave anisotropic tomography of the Alps. *Journal of Geophysical Research: Solid Earth*, *122*(6), 4509–4528. https://doi.org/10.1002/2016jb013831

Huang, T.-Y., Gung, Y., Kuo, B.-Y., Chiao, L.-Y., & Chen, Y.-N. (2015). Layered deformation in the Taiwan orogen. *Science*, *349*(6249), 720–723. https://doi.org/10.1126/science.aab1879

Institut de physique du globe de Paris (IPGP), & École et Observatoire des Sciences de la Terre de Strasbourg (EOST). (1982). GEOSCOPE, French global network of broad band seismic stations [Dataset]. https://doi.org/10.18715/GEOSCOPE.G

Istituto Nazionale di Oceanografia e di Geofisica Sperimentale—OGS. (2016). North-East Italy seismic network [Dataset]. *FDSN*. https://doi.org/10.7914/SN/OX

Jozi Najafabadi, A., Haberland, C., Le Breton, E., Handy, M. R., Verwater, V. F., Heit, B., & Weber, M. (2022). Constraints on crustal structure in the vicinity of the Adriatic Indenter (European Alps) from Vp and Vp/Vs local earthquake tomography. *Journal of Geophysical Research: Solid Earth*, *127*(2), e2021JB023160. https://doi.org/10.1029/2021jb023160

Kästle, E., El-Sharkawy, A., Boschi, L., Meier, T., Rosenberg, C., Bellahsen, N., et al. (2018). Surface wave tomography of the Alps using ambient-noise and earthquake phase velocity measurements. *Journal of Geophysical Research: Solid Earth*, *123*(2), 1770–1792. https://doi.org/10.1002/2017jb014698

Kästle, E., Molinari, I., Boschi, L., Kissling, E., & the AlpArray Working Group. (2022). Azimuthal anisotropy from eikonal tomography: Example from ambient-noise measurements in the AlpArray network. *Geophysical Journal International*, *229*(1), 151–170. https://doi.org/10.1093/gji/ggab453

Kästle, E. D., Soomro, R., Weemstra, C., Boschi, L., & Meier, T. (2016). Two-receiver measurements of phase velocity: Cross-validation of ambient-noise and earthquake-based observations. *Geophysical Journal International*, *207*(3), 1493–1512. https://doi.org/10.1093/gji/ggw341

Kästle, E. D., & Tilmann, F. (2023a). Data download and processing. (Scripts). https://doi.org/10.5281/zenodo.10428135

Kästle, E. D., & Tilmann, F. (2023b). baytomo2d. (Scripts). https://doi.org/10.5281/zenodo.10428121

Kästle, E. D., & Tilmann, F. (2023c). BayHunter AzAniso. (Scripts). https://doi.org/10.5281/zenodo.10428129

Keppler, R., Vasin, R., Stipp, M., Lokajíček, T., Petružálek, M., & Froitzheim, N. (2021). Elastic anisotropies of deformed upper crustal rocks in the Alps. *Solid Earth*, *12*(10), 2303–2326. https://doi.org/10.5194/se-12-2303-2021

Kern, H. (1990). Laboratory seismic measurements: An aid in the interpretation of seismic field data. *Terra Nova*, *2*(6), 617–628. https://doi.org/10.1111/j.1365-3121.1990.tb00127.x

Kern, H., & Schmidt, R. (1990). Physical properties of KTB core samples at simulated in situ conditions. *Scientific Drilling*, *1*(5), 217–223.

Koulakov, I., Kaban, M., Tesauro, M., & Cloetingh, S. (2009). P-and S-velocity anomalies in the upper mantle beneath Europe from tomographic inversion of ISC data. *Geophysical Journal International*, *179*(1), 345–366. https://doi.org/10.1111/j.1365-246x.2009.04279.x

Kövesligethy Radó Seismological Observatory, R. H. A. O. S. M. C. G. K., Geodetic and Geophysical Institute. (1992). Hungarian national seismological network [Dataset]. *GFZ Data Services*. https://doi.org/10.14470/UH028726

Kummerow, J., & Kind, R. (2006). Shear wave splitting in the Eastern Alps observed at the TRANSALP network. *Tectonophysics*, *414*(1–4), 117–125. https://doi.org/10.1016/j.tecto.2005.10.023

Kummerow, J., Kind, R., Oncken, O., Giese, P., Ryberg, T., Wylegalla, K., et al. (2004). A natural and controlled source seismic profile through the Eastern Alps: TRANSALP. *Earth and Planetary Science Letters*, *225*(1–2), 115–129. https://doi.org/10.1016/j.epsl.2004.05.040

Lamarque, G., Bascou, J., Maurice, C., Cottin, J.-Y., Riel, N., & Ménot, R.-P. (2016). Microstructures, deformation mechanisms and seismic properties of a Palaeoproterozoic shear zone: The Mertz shear zone, East-Antarctica. *Tectonophysics*, *680*, 174–191. https://doi.org/10.1016/j.tecto.2016.05.011

Le Breton, E., Handy, M. R., Molli, G., & Ustaszewski, K. (2017). Post-20 Ma motion of the Adriatic Plate: New constraints from surrounding orogens and implications for crust-mantle decoupling. *Tectonics*, *36*(12), 3135–3154. https://doi.org/10.1002/2016tc004443

Link, F., & Rümpker, G. (2019). Crustal anisotropy in the European Alps inferred from crustal phases in receiver functions and first implications for the mantle dynamics. In *Geophysical research abstracts* (Vol. 21).

Link, F., & Rümpker, G. (2021). Resolving seismic anisotropy of the lithosphere–asthenosphere in the Central/Eastern Alps beneath the SWATH-D network. *Frontiers in Earth Science*, *9*, 679887. https://doi.org/10.3389/feart.2021.679887

Lippitsch, R., Kissling, E., & Ansorge, J. (2003). Upper mantle structure beneath the Alpine orogen from high-resolution teleseismic tomography. *Journal of Geophysical Research*, *108*(B8), 2376. https://doi.org/10.1029/2002jb002016

Liu, C., Yao, H., Yang, H.-Y., Shen, W., Fang, H., Hu, S., & Qiao, L. (2019). Direct inversion for three-dimensional shear wave speed azimuthal anisotropy based on surface wave ray tracing: Methodology and application to Yunnan, southwest China. *Journal of Geophysical Research: Solid Earth*, *124*(11), 11394–11413. https://doi.org/10.1029/2018jb016920

Löberich, E., & Bokelmann, G. (2022). Mantle flow under the Central Alps: Constraints from shear-wave splitting for non-vertically-incident SKS waves. *Physics of the Earth and Planetary Interiors*, *329–330*, 106904. https://doi.org/10.1016/j.pepi.2022.106904

Lu, Y., Stehly, L., Brossier, R., Paul, A., & the AlpArray Working Group. (2020). Imaging Alpine crust using ambient noise wave-equation tomography. *Geophysical Journal International*, *222*(1), 69–85. https://doi.org/10.1093/gji/ggaa145

Lüschen, E., Lammerer, B., Gebrande, H., Millahn, K., Nicolich, R., Group, T. W., et al. (2004). Orogenic structure of the Eastern Alps, Europe, from TRANSALP deep seismic reflection profiling. *Tectonophysics*, *388*(1), 85–102. https://doi.org/10.1016/j.tecto.2004.07.024

Magrini, F., Lauro, S., Kästle, E., & Boschi, L. (2022). Surface-wave tomography using SeisLib: A Python package for multiscale seismic imaging. *Geophysical Journal International*, *231*(2), 1011–1030. https://doi.org/10.1093/gji/ggac236

Molinari, I., & Morelli, A. (2011). EPcrust: A reference crustal model for the European Plate. *Geophysical Journal International*, *185*(1), 352–364. https://doi.org/10.1111/j.1365-246x.2011.04940.x

Molinari, I., Obermann, A., Kissling, E., Hetényi, G., Boschi, L., & the AlpArray-EASI Working Group. (2020). 3D crustal structure of the Eastern Alpine region from ambient noise tomography. *Results in Geophysical Sciences*, *1*, 100006. https://doi.org/10.1016/j.ringps.2020.100006

Montagner, J.-P., & Nataf, H.-C. (1986). A simple method for inverting the azimuthal anisotropy of surface waves. *Journal of Geophysical Research*, *91*(B1), 511–520. https://doi.org/10.1029/jb091ib01p00511

Mroczek, S., Tilmann, F., Pleuger, J., Yuan, X., & Heit, B. (2023). Investigating the Eastern Alpine–Dinaric transition with teleseismic receiver functions: Evidence for subducted European crust. *Earth and Planetary Science Letters*, *609*, 118096. https://doi.org/10.1016/j.epsl.2023.118096

Nicolas, A., & Christensen, N. I. (1987). Formation of anisotropy in upper mantle peridotites—A review. *Composition, Structure and Dynamics of the Lithosphere-Asthenosphere System*, *16*, 111–123.

OGS (Istituto Nazionale di Oceanografia e di Geofisica Sperimentale), & University of Trieste. (2002). North-East Italy broadband network [Dataset]. *International Federation of Digital Seismograph Networks*. https://doi.org/10.7914/SN/NI

Okaya, D., Vel, S. S., Song, W. J., & Johnson, S. E. (2019). Modification of crustal seismic anisotropy by geological structures ("structural geometric anisotropy"). *Geosphere*, *15*(1), 146–170. https://doi.org/10.1130/ges01655.1

Paffrath, M., Friederich, W., Schmid, S. M., Handy, M. R., the AlpArray, & AlpArray-Swath D Working Group. (2021). Imaging structure and geometry of slabs in the greater Alpine area—A P-wave traveltime tomography using AlpArray seismic network data. *Solid Earth*, *12*(11), 2671–2702. https://doi.org/10.5194/se-12-2671-2021

Petrescu, L., Pondrelli, S., Salimbeni, S., Faccenda, M., & the AlpArray Working Group. (2020). Mantle flow below the central and greater Alpine region: Insights from SKS anisotropy analysis at AlpArray and permanent stations. *Solid Earth*, *11*(4), 1275–1290. https://doi.org/10.5194/se-11-1275-2020

Qorbani, E., Bianchi, I., & Bokelmann, G. (2015). Slab detachment under the Eastern Alps seen by seismic anisotropy. *Earth and Planetary Science Letters*, *409*, 96–108. https://doi.org/10.1016/j.epsl.2014.10.049

Qorbani, E., Zigone, D., Handy, M. R., Bokelmann, G., & AlpArray-EASI Working Group. (2020). Crustal structures beneath the Eastern and Southern Alps from ambient noise tomography. *Solid Earth*, *11*(5), 1947–1968. https://doi.org/10.5194/se-11-1947-2020

RESIF. (1995). RESIF-RLBP French Broad-band network, RESIF-RAP strong motion network and other seismic stations in metropolitan France [Dataset]. *RESIF—Réseau Sismologique et géodésique Français*. https://doi.org/10.15778/RESIF.FR

RESIF. (2018). CEA/DASE broad-band permanent network in metropolitan France [Dataset]. *RESIF—Réseau Sismologique et géodésique Français*. https://doi.org/10.15778/{RESIF}.RD

Rosenberg, C. L., Schneider, S., Scharf, A., Bertrand, A., Hammerschmidt, K., Rabaute, A., & Brun, J.-P. (2018). Relating collisional kinematics to exhumation processes in the Eastern Alps. *Earth-Science Reviews*, *176*, 311–344. https://doi.org/10.1016/j.earscirev.2017.10.013

Sadeghi-Bagherabadi, A., Vuan, A., Aoudia, A., Parolai, S., & the AlpArray and Swath-D Working Groups. (2021). High-resolution crustal S-wave velocity model and Moho geometry beneath the Southeastern Alps: New insights from the SWATH-D experiment. *Frontiers in Earth Science*, *9*, 641113. https://doi.org/10.3389/feart.2021.641113

Salimbeni, S., Malusà, M. G., Zhao, L., Guillot, S., Pondrelli, S., Margheriti, L., et al. (2018). Active and fossil mantle flows in the western Alpine region unravelled by seismic anisotropy analysis and high-resolution P wave tomography. *Tectonophysics*, *731*, 35–47. https://doi.org/10.1016/j.tecto.2018.03.002

Scharf, A., Handy, M., Favaro, S., Schmid, S. M., & Bertrand, A. (2013). Modes of orogen-parallel stretching and extensional exhumation in response to microplate indentation and roll-back subduction (Tauern Window, Eastern Alps). *International Journal of Earth Sciences*, *102*(6), 1627–1654. https://doi.org/10.1007/s00531-013-0894-4

Schippkus, S., Zigone, D., Bokelmann, G., AlpArray Working Group, & the ETHZ-Sed Electronics Lab. (2020). Azimuthal anisotropy in the wider Vienna basin region: A proxy for the present-day stress field and deformation. *Geophysical Journal International*, *220*(3), 2056–2067. https://doi.org/10.1093/gji/ggz565

Schmid, S. M., Bernoulli, D., Fügenschuh, B., Matenco, L., Schefer, S., Schuster, R., et al. (2008). The Alpine-Carpathian-Dinaridic orogenic system: Correlation and evolution of tectonic units. *Swiss Journal of Geosciences*, *101*(1), 139–183. https://doi.org/10.1007/s00015-008-1247-3

Schmid, S. M., Fügenschuh, B., Kissling, E., & Schuster, R. (2004). Tectonic map and overall architecture of the Alpine orogen. *Eclogae Geologicae Helvetiae*, *97*(1), 93–117. https://doi.org/10.1007/s00015-004-1113-x

Schuster, R., & Stüwe, K. (2008). Permian metamorphic event in the Alps. *Geology*, *36*(8), 603–606. https://doi.org/10.1130/g24703a.1

Serpelloni, E., Vannucci, G., Anderlini, L., & Bennett, R. (2016). Kinematics, seismotectonics and seismic potential of the eastern sector of the European Alps from GPS and seismic deformation data. *Tectonophysics*, *688*, 157–181. https://doi.org/10.1016/j.tecto.2016.09.026

Silver, P. G. (1996). Seismic anisotropy beneath the continents: Probing the depths of geology. *Annual Review of Earth and Planetary Sciences*, *24*(1), 385–432. https://doi.org/10.1146/annurev.earth.24.1.385

Slovenian Environment Agency. (1990). Seismic network of the Republic of Slovenia [Dataset]. *International Federation of Digital Seismograph Networks*. https://doi.org/10.7914/SN/SL

Soergel, D., Pedersen, H. A., Bodin, T., Paul, A., Stehly, L., & the AlpArray Working Group. (2022). Bayesian analysis of azimuthal anisotropy in the Alpine lithosphere from beamforming of ambient noise cross-correlations. *Geophysical Journal International*, *232*(1), 429–450. https://doi.org/10.1093/gji/ggac349

Spada, M., Bianchi, I., Kissling, E., Agostinetti, N. P., & Wiemer, S. (2013). Combining controlled-source seismology and receiver function information to derive 3-D Moho topography for Italy. *Geophysical Journal International*, *194*(2), 1050–1068. https://doi.org/10.1093/gji/ggt148

Swiss Seismological Service, ETH Zurich. (1983). National seismic networks of Switzerland [Dataset]. https://doi.org/10.12686/SED/NETWORKS/CH

Tilmann, F., Sadeghisorkhani, H., & Mauerberger, A. (2020). Another look at the treatment of data uncertainty in Markov chain Monte Carlo inversion and other probabilistic methods. *Geophysical Journal International*, *222*(1), 388–405. https://doi.org/10.1093/gji/ggaa168

Turner, F. J. (1942). Preferred orientation of olivine crystals in peridotites, with special reference to New Zealand examples. In *Transactions and proceedings of the royal society of New Zealand* (Vol. 72(3), pp. 280–300).

University of Genoa. (1967). Regional seismic network of north western Italy [Dataset]. *International Federation of Digital Seismograph Networks*. https://doi.org/10.7914/SN/GU

University of Leipzig. (2001). SXNET Saxon seismic network [Dataset]. *International Federation of Digital Seismograph Networks*. https://doi.org/10.7914/SN/SX

University of München, G. O., Department of Earth and Environmental Sciences. (2001). BayernNetz [Dataset]. *International Federation of Digital Seismograph Networks*. https://doi.org/10.7914/SN/BW

University of Trieste. (1993). Friuli Venezia Giulia Accelerometric Network [Dataset]. *International Federation of Digital Seismograph Networks*. https://doi.org/10.7914/SN/RF

University of Zagreb. (2001). Croatian seismograph network [Dataset]. *International Federation of Digital Seismograph Networks*. https://doi.org/10.7914/SN/CR

Wittlinger, G., Farra, V., Hetényi, G., Vergne, J., & Nábělek, J. (2009). Seismic velocities in Southern Tibet lower crust: A receiver function approach for eclogite detection. *Geophysical Journal International*, *177*(3), 1037–1049. https://doi.org/10.1111/j.1365-246x.2008.04084.x

Worthington, J. R., Hacker, B. R., & Zandt, G. (2013). Distinguishing eclogite from peridotite: EBSD-based calculations of seismic velocities. *Geophysical Journal International*, *193*(1), 489–505. https://doi.org/10.1093/gji/ggt004

Wüstefeld, A., Bokelmann, G., Barruol, G., & Montagner, J.-P. (2009). Identifying global seismic anisotropy patterns by correlating shear-wave splitting and surface-wave data. *Physics of the Earth and Planetary Interiors*, *176*(3–4), 198–212. https://doi.org/10.1016/j.pepi.2009.05.006

Xie, J., Ritzwoller, M. H., Brownlee, S., & Hacker, B. (2015). Inferring the oriented elastic tensor from surface wave observations: Preliminary application across the western United States. *Geophysical Journal International*, *201*(2), 996–1021. https://doi.org/10.1093/gji/ggv054

Xie, J., Ritzwoller, M. H., Shen, W., & Wang, W. (2017). Crustal anisotropy across eastern Tibet and surroundings modeled as a depth-dependent tilted hexagonally symmetric medium. *Geophysical Journal International*, *209*(1), 466–491.

ZAMG—Zentralanstalt für Meterologie und Geodynamik. (1987). Austrian seismic network [Dataset]. *International Federation of Digital Seismograph Networks*. https://doi.org/10.7914/SN/OE

Zertani, S., John, T., Tilmann, F., Motra, H. B., Keppler, R., Andersen, T. B., & Labrousse, L. (2019). Modification of the seismic properties of subducting continental crust by eclogitization and deformation processes. *Journal of Geophysical Research: Solid Earth*, *124*(9), 9731–9754. https://doi.org/10.1029/2019jb017741

Zertani, S., Vrijmoed, J. C., Tilmann, F., John, T., Andersen, T. B., & Labrousse, L. (2020). P wave anisotropy caused by partial eclogitization of descending crust demonstrated by modeling effective petrophysical properties. *Geochemistry, Geophysics, Geosystems*, *21*(6), e2019GC008906. https://doi.org/10.1029/2019gc008906

Zhao, L., Paul, A., Malusà, M. G., Xu, X., Zheng, T., Solarino, S., et al. (2016). Continuity of the Alpine slab unraveled by high-resolution P wave tomography. *Journal of Geophysical Research: Solid Earth*, *121*(12), 8720–8737. https://doi.org/10.1002/2016jb013310